NASA Technical Paper 1793

Determination of the Hypersonic-Continuum/Rarefied-Flow Drag Coefficient of the Viking Lander Capsule 1 Aeroshell From Flight Data

Robert C. Blanchard and Gerald D. Walberg

DECEMBER 1980

NASA

NASA Technical Paper 1793

Determination of the Hypersonic-Continuum/Rarefied-Flow Drag Coefficient of the Viking Lander Capsule 1 Aeroshell From Flight Data

Robert C. Blanchard and Gerald D. Walberg
Langley Research Center
Hampton, Virginia

NASA
National Aeronautics
and Space Administration

Scientific and Technical
Information Branch

1980

SUMMARY

The entry of the Viking Lander Capsule 1 into the predominantly carbon dioxide atmosphere of Mars provided the first opportunity to obtain full-scale aerodynamic flight measurements in the high-speed, low-density regime. These data are also of particular scientific importance because of their potential impact on the wavy nature of the Martian upper-atmosphere temperature profile previously deduced from wind-tunnel aerodynamics and in-flight acceleration measurements. Results are presented from an investigation to determine the aerodynamics of the Viking Lander Capsule 1 principally with flight measurements from pressure instruments, accelerometers, and a mass spectrometer. Included is a detailed examination of the flight data and the processing techniques of each of the types of measurement over the complete spectrum of flight regimes from the hypersonic continuum to the free molecule flow. In the hypersonic continuum, combined processing of pressure and acceleration data provided an unambiguous determination of the aerodynamics. Comparisons of these aerodynamics with ground-based ballistic-range and CF_4 wind-tunnel continuum coefficients are made. The free-molecule-flow drag coefficient was solved for with an indirect technique since acceleration noise prevented a direct solution. Theoretical calculations based upon molecular-beam experimentation in the free-molecule-flow regime are applied to assess the validity of the value obtained from the flight data. Experimental data for spheres were scaled and used to define the drag variation in the slip-flow regime since no atmosphere measurements were available for direct calculations. This allowed for the complete definition of the drag coefficient in the rarefied-flow regime. The flight-derived drag coefficient was used to calculate the atmosphere structure and results are compared with previously determined estimates.

Comparison of the flight-derived drag coefficients with ground-test data generally showed good agreement in the hypersonic-continuum-flow regime except for Reynolds numbers from 10^5 to 10^3, for which an unaccountable difference between flight- and ground-test data of about 8 percent existed. The flight-derived drag coefficient in the free-molecule-flow regime was considerably larger than that previously calculated with classical theory. The general character of the previously determined temperature profile was not changed appreciably by the results of this investigation; however, a slightly more symmetrical temperature variation at the highest altitudes was obtained.

INTRODUCTION

Separate groups at the Jet Propulsion Laboratory (JPL), Ames Research Center (ARC), and Langley Research Center (LaRC) analyzed the first Viking lander capsule atmospheric structure and trajectory data in near real time for the purpose of atmospheric certification. The ARC initial results were formally reported (ref. 1). Although comparisons between the different sets of data were adequate for purposes of successfully targeting the second Viking lander capsule, a striking "waviness" superimposed on a near isothermal trend

appeared in the temperature profile above altitudes of about 50 km in all three separate data reductions. Additional analysis of the first lander capsule entry data (ref. 2) and analysis of the second lander data (ref. 3) indicated the same wavy nature of the temperature profile above about 50 km. Seiff and Kirk's interpretation of these waves as being due to diurnal thermal tides, analyzed for Mars by Zurek (ref. 4) and for Earth by others (ref. 5), is the prevailing explanation for this phenomenon. However, this phenomenon occurs at altitudes where the entry vehicle experiences high speeds and relatively low acceleration readings. In this high-altitude region, wind-tunnel aerodynamic data must be used with the acceleration data to determine temperatures. This fact precipitated a lengthy investigation to reexamine, in detail, the region from about 50 km to 130 km to see if the previously deduced temperature profile could be caused by flight-aerodynamics phenomena rather than by actual temperature variations in the Martian atmosphere. The initial examination of the data indicated that the vehicle aerodynamic characteristics might be extracted solely from the flight data. If this was the case, then not only could the atmospheric data be independently verified, but it would provide the first flight-test data on a conical blunt body in a nonair medium. In order to accomplish this goal, a different approach from previous investigations in the data reduction process was employed. This approach used the additional measurements of stagnation pressure and mass-spectrometer number densities in techniques that combined them with the accelerometer data to independently obtain aerodynamic force coefficients in the hypersonic-continuum-flow and the free-molecule-flow regime. Experimental data for spheres were used to define the shape of the drag curve between the hypersonic-continuum-flow and the free-molecule-flow regime, and an iterative procedure was used to fit the data and derive a complete, smooth variation of drag coefficient. This process resulted in aerodynamic drag data for a 70° conical blunt body from the hypersonic-continuum-flow to the free-molecule-flow regime. These data were also used to calculate the atmospheric structure for Mars. The resulting temperature profile is compared with that previously obtained. This paper describes the analyses and presents the results of the investigation to determine the hypersonic-continuum/rarefied-flow aerodynamics and atmospherics from the Viking Lander Capsule 1 data.

SYMBOLS

$\vec{A}$	acceleration vector
A_x, A_y, A_z	components of $\vec{A}$
C_A	axial-force coefficient
C_D	drag coefficient
C_L	lift coefficient
C_N	normal-force coefficient, positive in the positive z-direction
C_p	hypersonic stagnation-pressure coefficient, $\frac{P_s}{(1/2)\rho_\infty V_\infty^2}$

d	molecule elastic-sphere equivalent diameter
E	molecular energy flux
g_E	Earth gravitational acceleration ($g_E = 9.087$ m/s^2)
K	proportionality constant for molecular-velocity distribution law
k	Boltzmann's constant
L/D	lift-drag force ratio
$\bar{l}$	equivalent elastic-sphere mean free path
M	Mach number
m	vehicle mass
$\mathcal{M}$	mean molecular weight
N_{Kn}	Knudsen number
N_o	Avogadro's number, 6.0249×10^{23}
N_{Re}	Reynolds number
N_{ref}	number of reemitted molecules per unit time
n	measured number density
n_t	total number density
P	pressure
p	angular rate about the x-axis
q	angular rate about the y-axis
R	gas constant
r	angular rate about the z-axis
S	molecule-speed ratio
s	vehicle reference area
T	temperature
V	relative velocity of vehicle
$\vec{X}$	vector location with respect to center of gravity

X,Y,Z	components of $\vec{X}$
α	accommodation coefficient
α_2	partial accommodation coefficient
$\Delta\vec{A}$	acceleration vector produced by rotations about the center of gravity
$\Delta\theta$	change in angular orientation
ε	mean molecular energy
η	total angle of attack
μ	molecular-mass ratio (incident-to-surface molecular mass)
ν	exponent for angle reflection law
ρ	mass density
θ	angular orientation
σ	tangential-momentum accommodation coefficient
σ'	normal-momentum accommodation coefficient
ϕ	molecular-beam half-angle width
$\dot{\Omega}$	angular acceleration matrix

Subscripts:

b	body axis
c	continuum flow
fm	free molecule flow
i	incident molecule
m	measurement
o	maximum value
p,q,r	components in the p-, q-, or r-directions
per	periodic component
ref	reemitted (or reflected) molecule
s	stagnation

se	secular component
w	reflected molecule at wall temperature
x	component along x-axis
∞	free-stream conditions

A dot over a symbol indicates differentiation with respect to time.

APPROACH

An ideal experiment for obtaining the aerodynamic-force coefficients from entry-flight data is one which includes simultaneous measurements of acceleration and atmospheric information, primarily measurements of density. Under these conditions, the product $C_A\rho_\infty$ can be unambiguously separated in the following equation:

$$C_A\rho_\infty = \frac{-2A_x}{V^2(s/m)} \tag{1}$$

On the Viking lander capsule, particularly in the rarefied-flow flight regimes, this overlap of acceleration and atmospheric measurements did not occur. Figure 1 is a sketch of the approximate useful limits of each of the three principal measurements relative to the flow regimes used in this study.

In the hypersonic-continuum-flow regime for which both stagnation pressure and accelerations were available, the aerodynamic coefficients were determined directly from calculated values of the hypersonic stagnation-pressure coefficient, which varied little over the Mach number range of the data.

The acceleration data extended well into the slip-flow flight regime, but it did not overlap the mass-spectrometer density data. Consequently, a direct determination of the free-molecule-flow aerodynamic coefficient was not possible. However, since the altitude gap between the acceleration-data and the mass-spectrometer-data limits was relatively small (approximately 20 km), it was possible to obtain an estimate of the coefficient by establishing a continuity relation between the two sets of data by assuming an essentially isothermal atmospheric region between them. Upon establishment of a coefficient value from the data, free-molecule-flow theories were applied with the Viking lander capsule configuration and the environment as measured. The flight-data value was compared with the theoretical calculations to establish its reasonableness.

The slip-flow regime contained no atmospheric information corresponding to the accelerometer measurements, and the gap between the two atmospheric measurements was fairly large (approximately 50 km). In this regime, the approach taken consisted of applying a scaled drag-coefficient variation

obtained for spheres in ground-based test facilities, matching both the determined free-molecule-flow drag coefficient value and the hypersonic-continuum-flow value. An iterative procedure was then used to obtain the best fit of all the data over the whole range from the continuum to the free-molecule-flow regime.

ENTRY-FLIGHT SEQUENCE

At 8:31 GMT on July 20, 1976, the Viking Lander Capsule 1 was separated from the Viking orbiter to begin its 18 200-km journey to the surface of Mars. The onboard, preprogrammed sequence of events which is pertinent to the discussions of data processing and spacecraft orientation for the descent period will be briefly reviewed. Further details can be obtained from reference 6. Deorbit began after a 4-min coast period following separation. At this time the lander capsule performed a preprogrammed orientation maneuver in preparation for a deorbit maneuver which consisted of an inertially controlled engine firing of the reaction control system (RCS). The objective of this maneuver was to deliver the lander capsule to the entry point (defined as 243.8 km (800 000 ft) from the surface) with the predetermined proper entry trajectory state, that is, a relative velocity of 4.42 km/s and a relative velocity path angle of -17.63°. At the entry point, which was determined by an onboard computer clock, the vehicle was oriented to its predetermined trim angle of attack of -11.1° in preparation for entry into the Martian atmosphere. This attitude was maintained by the RCS until $0.05g_E$ were sensed, at which time the vehicle was set free to seek its natural trim attitude but was constrained in attitude rate change to less than 1 deg/s by the onboard navigation rate-damping system. This $0.05g_E$ acceleration mark initiated the first phase of a three-phase deceleration entry system used to successfully soft-land an instrumented vehicle on the planet's surface.

INSTRUMENTATION AND VEHICLE DESCRIPTION

The lander capsule contained several scientific instruments with which to gather information on the properties of the Martian environment as the lander traversed the atmosphere. Figure 2 contains detailed views of the Viking Lander Capsule 1 and the relative locations of the various instruments contained within. The aeroshell structure consisted of a 70° half-angle cone composed of a phenolic honeycomb material. This ablative structure contained two upper-atmosphere instruments (the retarding potential analyzer (RPA) and the upper-atmosphere mass spectrometer (UAMS)), two lower-atmosphere sensing devices (a temperature probe automatically deployed at a velocity of 1.1 km/s and a stagnation-pressure transducer), and other measurement devices. These included the high-altitude antenna and four pressure transducers; which were used in both the reconstruction of the trajectory and the postflight engineering evaluations. The inertial reference unit (IRU), a package which contained three principal-axis accelerometers and gyros, a redundant skewed gyro, and a redundant axial accelerometer, was mounted on the hexagonal frame of the lander. The projection of the location of the IRU into the YZ-plane was about (0.3 m, -1.0 m) from the center of gravity, which was at (0, -0.046 m) from the axis of symmetry. The selection of this center of gravity away from the axis of symmetry provided a nose-down

(-11.1°) angle of attack and a positive lift (L/D ≈ 0.18). The assembled 3.5-m-diameter lander capsule weighed 980.8 kg at entry, and yaw and pitch were controlled by a crossed array of eight dual-operated 15.21-N (3.42-lb) thrusters. Roll was controlled by redundant coupled pairs of identical thrusters, as shown in figure 2.

DATA PREPARATION

Accelerometer and Gyro Data

The accelerometer data received on the entry into the Martian atmosphere of the Viking Lander Capsule 1 have been examined in detail in order to prepare records of aerodynamic-induced acceleration. This preparation consisted of smoothing each channel with a moving cubic polynomial, removal of the thrust-induced axial input, and removal of biases as determined just prior to sensing atmospheric effects. Analysis of the gyro data indicate that accelerations induced by angular motions of the IRU about the vehicle's center of gravity did not generate a significant contamination signal of the smooth aerodynamic acceleration records. The detailed description of the preparation processes for these data is given in appendix A.

Pressure Data

The flight stagnation-pressure data used in the determination of the hypersonic-continuum-flow aerodynamic coefficient has been prepared in a manner similar to the accelerometer and gyro data. The preparation consisted of removing the zero-shift, smoothing with a second-order polynomial, and applying minor corrections to account for low-density-orifice effects. The sensor output contained dual channels with resolutions of 0.15 and 0.81 millibar (1.0 bar = 100.0 kPa). An analysis of the smaller resolution output channel with the trajectory provided an altitude estimate of about 75 km as the upper limit of useful information from this sensor. A detailed description of the data preparation process, the sensor threshold analysis, and the data record is given in appendix B.

Mass-Spectrometer Data

Unlike the preceding data, no separate smoothing was applied to the reported free-stream neutral-species concentrations. The preparation of the mass-spectrometer data from the lander entry consisted mainly of calculating total mass density and mean molecular weight of the atmosphere at the upper altitudes from about 128 to 200 km. The lowest five data points, from about 128 to 150 km, were of the most interest in attempting to extract the free-molecule-flow aerodynamic coefficient described later. Of these data, the lowest few data points were in the fringes of the slip-flow regime based upon analysis of the flow regimes described later. Consequently, these few data points were slightly biased toward values higher than for free-stream conditions. A brief description of the data-acquisition period, the details of

the calculations, and the table of results from the data are presented in appendix C.

ANALYSIS OF FLIGHT DATA

Trajectory Parameters

The relative velocity-altitude profile of the lander is given in figure 3. The velocity was obtained from a separate analysis of the postflight trajectory-reconstruction process (ref. 7). This process primarily involved the integration of the acceleration records and use of the available redundant measurement data (e.g., altimeter, terminal descent landing radar, and the landed-radio position-determination results) as information for solving the initial-state conditions. This process was independent of atmospheric properties and vehicle aerodynamics. The velocity profile presented was used in the subsequent calculations.

Also included in figure 3 is the approximate average free-stream Mach number variation for the range of altitudes of this investigation (from about 30 to 150 km). The average atmospheric temperature and a constant value of the ratio of specific heat of 1.3 were used in the calculation. Above 80 km the variation is considered only an approximation and is indicated as such by a dashed line.

Entry Flow Regimes

An important consideration in determining the aerodynamic coefficients of an entry vehicle traveling at high speeds in a low-density medium is the determination of the flow regime in which the vehicle resides. An acceptable classification of hypersonic flight regimes is that proposed in references 8 and 9. The boundaries of the flow regimes are usually defined by the free-stream Knudsen number, but since the Mach number undergoes only small variations throughout most of the low-density-flow regimes for an entry such as that of the Viking lander capsule, it is possible to also define the flow-regime boundaries in terms of free-stream Reynolds number, as given by Probstein in reference 9. Thus,

$$N_{Kn,\infty} \sim M_{\infty}/N_{Re,\infty} \tag{2}$$

Figure 4 indicates the boundaries of the various flow regimes presented in terms of both Knudsen number and Reynolds number for the Viking lander capsule entry. Also presented is a typical drag-coefficient variation as a function of these parameters to show the relative magnitude of entry vehicle drag in the various flow regimes. The slip-flow regime defined in figure 4 is a collection of other subdivided flow regimes described by Probstein. The term "slip flow" refers to the fact that the usual continuum assumption of zero tangential velocity at the vehicle surface does not apply for these rarefied flows. For this investigation,

it is adequate to define only these three regimes because of the availability of measurement data.

Some knowledge of atmospheric properties was required in order to estimate which flow regime the vehicle was in at various altitudes. For the Viking lander capsule, the mass-spectrometer data provided a measure of the number densities of various atmospheric species, and these data were used to compute the equivalent elastic-sphere mean free path (ref. 10) through the relation

$$l = \frac{1}{\sqrt{2}\pi n d^2} \tag{3}$$

where n is the measured number density and d is the elastic-sphere equivalent diameter of the molecule determined experimentally in the laboratory. For CO_2, the predominant species in the region of interest, $d \approx 4.59 \times 10^{-8}$ cm. The results of the calculation of mean free path for collisions between CO_2 molecules are shown in figure 5. Other species collisions were neglected since their contributions were minimal in this preliminary estimate. A linear regression extrapolation with the last four mass-spectrometer points (shown by the dashed line in fig. 5) was used as a temporary means to extend the data to lower altitudes. This was not entirely unreasonable since earlier analysis indicated a nearly isothermal temperature region at these altitudes. As shown in figure 5, $N_{Kn,\infty} \approx 50$ (corresponding to the free-molecule-flow boundary) occurs near an altitude of 140 km and the hypersonic-continuum-flow boundary $N_{Kn} \approx 2 \times 10^{-3}$ begins near an altitude of 80 km. Hence, the Viking lander capsule drag coefficient would be expected to undergo a significant change (similar to that shown in fig. 4) between the altitudes of 140 and 80 km.

Determination of Force Coefficients

Atmospheric flight data from high-speed entry vehicles usually prohibit completely independent measurements of ambient atmospheric conditions. (Ambient conditions are disturbed by the vehicle's motion, and the vehicle is the measurement platform.) Thus, in general, the product $C_D\rho_\infty$ cannot be directly separated and the coefficient solved for explicitly in the aerodynamic-force equation. However, in this case it was possible to use the atmosphere-dependent measurement data (e.g., mass-spectrometer and pressure data) with the acceleration and trajectory information so that atmospheric parameters are introduced indirectly into the coefficient-extraction process with an iterative scheme. Refinements to the results can be made by iterating between all the elements of the problem.

In order to extract all the usable information from the Viking lander capsule acceleration measurements it was necessary to estimate drag coefficients at altitudes up to about 100 km. However, above 75 km, the flight stagnation-pressure data were not sufficiently accurate to allow calculation of the drag coefficient. Accordingly, the following general approach to estimating the drag-coefficient variation was used:

1. The hypersonic-continuum-flow drag coefficient was calculated (for altitudes up to 75 km) from the flight stagnation-pressure and acceleration measurements.

2. From continuity between acceleration and mass-spectrometer data and from examination of free-molecule-flow theories, a value for the free-molecule-flow drag coefficient was obtained for altitudes down to about 140 km.

3. Previously published experimental data on slip-flow drag coefficients for spheres were used to define the variation of the drag coefficient from its continuum value to its free-molecule-flow value.

This procedure provided the complete drag variation from the hypersonic-continuum-flow regime into free-molecule-flow regime. The details of the process for each flow regime and the results of the calculations for the overall drag variations are discussed separately.

Hypersonic continuum flow.- The determination of the body-axis aerodynamic-force coefficients from the acceleration and stagnation-pressure data was made from the following equations:

$$\left.\begin{aligned} C_A &= -A_x \frac{C_{p^m}}{P_s s} \\ C_N &= A_z \frac{C_{p^m}}{P_s s} \end{aligned}\right\} \qquad (4)$$

The measured acceleration and pressure data used in these calculations were those after the aforementioned preprocessing had been applied using both the high-range and low-range pressure measurements. The error incurred by not including the static pressure in the equations was negligible since it was small in comparison to the stagnation pressure.

The pressure coefficient used to determine the axial- and normal-force coefficients of the lander aeroshell was obtained from a combination of theoretical and experimental data. At altitudes below approximately 40 km, the shock layer over the aeroshell forebody was expected to be in chemical equilibrium. Accordingly, pressure coefficients were computed for a range of flight conditions using the computer program of reference 11. In this calculation, the Rankine-Hugoniot equations across a normal shock were solved under the assumption of chemical equilibrium. All significant chemical species in the Martian atmosphere and their dissociation products were included. The postshock flow was brought to rest adiabatically to compute the stagnation conditions at the vehicle surface. For these calculations, the composition of the Martian atmosphere was taken to be that reported in reference 12, approximately 95 percent carbon dioxide (CO_2), 3 percent nitrogen (N_2), and 2 percent Argon (Ar) by volume. At altitudes between 26 and 40 km, where equilibrium flow prevailed,

the pressure coefficient was found to be nearly constant at a value of approximately 1.96. At altitudes above 40 km, experimental data obtained in the Langley Expansion Tube (ref. 13) indicated a departure from chemical equilibrium. This departure produced a reduction of approximately 5 percent in the pressure coefficient, which was accounted for by an approximate correction based on the data presented in reference 13. The resulting variation of C_p with altitude is presented in figure 6. This variation with altitude was established by correlating the values of C_p with density obtained by combining the accelerometer data with an initial estimate of the drag coefficient.

Additional calculations were performed to provide the wind-vector aerodynamic coefficients. These included the application of the following equations:

$$\left.\begin{aligned} C_D &= C_A \cos \eta + C_N \sin \eta \\ C_L &= -C_A \sin \eta + C_N \cos \eta \end{aligned}\right\} \qquad (5)$$

where η is the total angle of attack as deduced from the gyro data in the trajectory reconstruction process. The wind-vector force coefficients obtained in this manner are presented in figure 7. The angle of attack used in the calculations are also included.

Free molecule flow.- A twofold approach was taken to determine the free-molecule-flow drag coefficient of this entry vehicle. First, a continuity argument between the mass-spectrometer data and acceleration data was established, and second, the drag and lift coefficients were calculated using free-molecule-flow theory to reinforce the validity of the flight-data value.

Continuity was established between density obtained from mass-spectrometer data and from density inferred from the accelerometers to bridge the 20-km altitude gap between the two types of data. This required two assumptions. First, density, on a logarithmic scale, was assumed to vary linearly with altitude. That is, under mixed atmospheric conditions temperature was assumed to be isothermal. Second, it was assumed that the velocity did not appreciably change over this interval. To the first order, these assumptions were reasonable based upon work reported earlier. Then, from the force equation,

$$\rho \approx \text{Constant}\left(\frac{A_x}{C_A}\right)$$

or

$$\frac{\Delta\rho}{\rho} \approx -\frac{\Delta C_A}{C_A} \qquad (6)$$

That is, an incremental decrease in C_A would produce a predictable increase in density for a given A_X. Density-altitude profiles were calculated for various assumed values of C_A and extrapolated into the region where mass-spectrometer data existed since, as stated earlier, a net change in C_A was equivalent to a net change in ρ throughout the interval. The results of the calculations for constant values of C_A from 3.0 to 1.5 are shown in figure 8. The last four mass-spectrometer data points are also shown in the figure. Clearly shown is the 20-km gap between the two data types for which the accelerometer noise prohibited a direct coefficient calculation as mentioned earlier. A value of 2.5 for the free-molecule-flow axial coefficient could fulfill the requirement of density continuity and thus provide the merger into the hypersonic-continuum-flow value without unduly complicating the atmosphere structure.

In addition to the flight-data analysis, a review of free-molecule-flow theory was carried out in order to define the range of free-molecule-flow drag coefficients that can be believably predicted for the Viking lander aeroshell within the current state of the art. This review, presented in appendix D, led to the selection of the theory of Hurlbut and Sherman (ref. 14), which uses the Nocilla wall reflection model (ref. 15), as a realistic description of the Viking lander capsule flow conditions. When this theory was applied to the Viking lander capsule aeroshell, free-molecule-flow drag coefficients ranging from approximately 2.54 to 2.63 were obtained depending on the value chosen for the accommodation coefficient. These values are significantly higher than the value of 2.20 which corresponds to the classical fully accommodated diffuse-reflection model. In the absence of valid normal acceleration data, an approximate value of C_D corresponding to the extrapolated flight value of C_A was deduced by using the theoretical free-molecule value $C_N/C_A \approx 0.26$ in the preceding body-to-wind-axis transformation. The corresponding value of C_D is 2.58. Based upon the analysis presented in appendix D and the preceding continuity argument with the data, values of 2.50 to 2.70 were selected as the most probable range of free-molecule-flow drag coefficients. However, it is difficult to assign a meaningful formal uncertainty value to this range of coefficients, although the data favors the lower value corresponding to the diffuse-reflection condition.

Slip flow.- There were no atmospheric measurements made on the Viking lander capsule to provide a direct calculation of the aerodynamics in the slip-flow flight regime. As reported earlier, the hypersonic-continuum-flow aerodynamics were determined from both pressure and acceleration measurements to an altitude of about 75 km. In the free-molecule-flow regime (above about 140 km), the aerodynamic coefficient can be inferred by imposing a continuity assumption between mass-spectrometer and accelerometer data. Although the accelerometer data appears valid (i.e., not too noisy) to about 110 km, no corresponding atmospheric measurements were available to uniquely separate the product $C_A\rho_\infty$ in the force equations at these altitudes. Thus, an indirect approach was adopted to estimate the change in the drag coefficient through this regime. In this approach, it was assumed that throughout the slip-flow regime the drag-coefficient trend for the Viking lander capsule aeroshell was similar to that reported for spheres. The particular drag-coefficient variation used was that proposed by Kinslow and Potter (ref. 16). This variation is presented in dimensionless form in figure 9. For Reynolds numbers greater than about 50 the

variation represents a curve fit to experimental data obtained at Mach numbers of approximately 11 and low ratios of wall to free-stream stagnation temperature. For Reynolds numbers less than 50 the curve resulted from a first-collision theory analysis that was empirically adjusted to match the available experimental data.

Overall drag-coefficient variation.- In general, the data obtained during the Viking lander capsule entry were not sufficient to allow the independent determination of the aerodynamic coefficients and the atmospheric density throughout the entire entry. For instance, the application of the sphere drag coefficient in the slip-flow regime required a determination of Reynolds number, which in turn required a knowledge of the free-stream density. Accordingly, an iterative procedure was used to arrive at simultaneous best-estimates of aeroshell aerodynamic coefficients and atmospheric-density profiles. The iteration procedure was as follows:

1. An initial estimate of the atmospheric-density profile was obtained by joining, in a smooth manner, the high-altitude (greater than 128 km) mass-spectrometer data with densities calculated from the accelerometer data combined with a nominal hypersonic-continuum-flow drag coefficient derived from an average of the wind-tunnel values. Corresponding profiles of atmospheric pressure and temperature were obtained from integration of the barometric equation and the application of the perfect gas law, respectively. With this atmospheric information, Reynolds number and Mach number were calculated as functions of altitude. The gas properties for these calculations were obtained from data in reference 17.

2. This density-altitude profile was used to establish an initial variation of the previously calculated values of hypersonic stagnation-pressure coefficient C_p with altitude. (This step was included more for completeness rather than necessity since the variation in C_p was less than 2 percent in the region investigated).

3. The hypersonic-continuum-flow aerodynamic coefficients were calculated (for altitudes up to approximately 75 km) from C_p and the measured stagnation-pressure and acceleration data.

4. The drag coefficient in the slip-flow regime was obtained from figure 9. The ordinate on this figure was normalized to the difference between the free-molecule-flow and hypersonic-continuum-flow drag coefficients obtained for spheres. The slip-flow drag coefficient is therefore scaled according to the values of the drag coefficient at either end of the Reynolds number range derived from step 1 and used as the abscissa in this figure. The free-molecule-flow drag coefficient was fixed at either 2.50 or 2.70 and remained so for all iterations whereas the hypersonic-continuum-flow drag coefficient was adjusted for each iteration.

5. The complete drag-coefficient variation obtained from steps 2 to 4 was used to deduce from the accelerometer data an improved approximation to the density profile below 110 km.

6. The density profile from step 5 was joined with mass-spectrometer data to produce an improved overall density profile.

7. Atmospheric pressure and temperature profiles corresponding to the density profile from step 6 were computed from integration of the barometric equation and application of the perfect gas law, respectively.

8. Steps 2 to 7 were repeated until converged values for the drag coefficient and the atmospheric profiles were obtained.

The resultant overall drag-coefficient variation is presented as a function of altitude in figure 10 for the upper-bound free-molecule-flow drag coefficient (i.e., $C_D = 2.70$). Included on a separate graph in this figure is the variation of free-stream Reynolds number with altitude. Also included on this graph of drag-coefficient variation is the output of step 3 from the preceding process after the final iteration. The Reynolds numbers computed from the last five mass-spectrometer data values are included for interpolation purposes and to identify the flow region where no flight data exists.

Figure 11 is a graph of the final product of this investigation, that is, a description of the complete variation of the drag coefficient with free-stream Reynolds number. Essentially, this graph contains the same information as the two graphs in figure 10. Included in the figure are the flow regimes and the approximate thresholds (i.e., useful limits) of the data used to determine the drag-coefficient variation shown. These are shown to emphasize the flow regimes for which special steps were taken to provide a complete description of the coefficient variation, for instance, the slip-flow regime.

Comparison With Ground-Test Data

Several series of experimental aerodynamic tests were performed on the Viking lander capsule aeroshell configuration prior to flight. Besides tests in air, which consistently produced coefficients about 5 to 10 percent less than nonair tests, real-gas composition effects were included in wind-tunnel tests at both LaRC and ARC. The LaRC tests (ref. 18) were carried out at $M_\infty \approx 6$ and $N_{Re,\infty} \approx 3 \times 10^6$ and were conducted in CF_4 to more closely match the expected ratio of densities across the shock at hypersonic-continuum-flow flight conditions typical of the Viking lander capsule entry. The ARC tests (ref. 19) were conducted in CO_2 at the ballistic-range facility which has a capability of projecting scale models at speeds equivalent to the Viking lander capsule entry speed of 4.5 km/s and a capability of making drag measurements at very low Reynolds numbers (in the hundreds). These data provide the basis for comparison of the wind-tunnel and ballistic-range drag coefficients with the flight-derived drag coefficients discussed in the previous section. Figure 12 shows the variation of flight-derived C_D with free-stream Reynolds number reproduced from figure 11 (solid curve) compared with the aforementioned ground-test data. Also included in the figure is the drag-coefficient variation used in the calculation of the Martian atmospheric characteristics reported in reference 2 (dashed curve). Direct comparisons of drag-coefficient data with the ballistic-range data greater than a Reynolds number of about 1×10^5 (corresponding to an altitude of about 60 km) indicates excellent agreement, that is,

a difference of less than 2 percent. Above this altitude (as $N_{Re,\infty}$ decreases), the results show a difference of about 8 percent, which may be regarded as acceptable considering the experimental difficulties in acquiring the ballistic-range data in this regime. However, as shown in the figure, the abrupt drag-coefficient change observed in the ballistic-range tests is not observed in the flight data. Initially it was postulated that this coefficient change was due to a laminar-turbulent transition in the wake flow (ref. 2). This is not probable since wake pressure changes do not significantly influence drag at these velocities. Further, no mechanism immediately arises which allows this magnitude of drag change to occur in the flight results. Additional investigation will be required to isolate the cause for this difference. However, except for this difference, the hypersonic-continuum-flow values of the flight-derived drag coefficient are consistent with data obtained from the ballistic-range and CF_4 wind-tunnel data.

Total angle-of-attack calculations indicated that the orientation of the vehicle to the flow was not at a constant 11.1°. (See fig. 7.) Thus, the flying conditions of the actual vehicle were slightly different from the ground-tested conditions compared here. These differences are believed to be well within the limits of the expected error since a 1° change in angle of attack produces only about 1 percent change in drag coefficient in the flight regime under study.

The differences between the flight-derived coefficients and the model used in reference 2 can be seen by comparing the solid and dashed curves in figure 12. The model of reference 2 relied directly upon the tunnel observations and assumed a free-molecule-flow drag coefficient of 2.00, which is considerably lower than the values of 2.50 to 2.70 derived in this investigation. Also note that the drag coefficient begins to change from the free-molecule-flow value at a Reynolds number of about 5 in the current investigation whereas this change did not occur until a Reynolds number of about 30 for the dashed curve. The drag-coefficient variation from reference 2 through the slip-flow regime is based on drag data for spheres reported by Masson et al. (ref. 20). Of course, these coefficient differences would produce differences in the atmospheric properties since at these altitudes atmospheric properties are inferred from interpretation of acceleration measurements and vehicle drag coefficients.

MARTIAN ATMOSPHERIC PROFILES

The atmospheric state variables were calculated by transforming acceleration into density with the aerodynamic force equation given by

$$\rho = \frac{-2A_x}{C_A V^2 (s/m)} \tag{7}$$

where C_A is the previously discussed flight-determined axial-force coefficient, rather than the wind-tunnel estimate. This resulted in a table of density versus time which, combined with the trajectory-reconstruction process, produced

an altitude profile of density. Atmospheric pressure and temperature profiles were calculated from integration of the barometric equation and application of the perfect gas law, respectively. Application of the aforementioned aerodynamic variation (with the free-molecule-flow drag coefficient of 2.70) produced the temperature results shown in figure 13 corresponding to the acceleration data. The corresponding density and pressure profiles are not shown since temperature, the ratio of these variables, presents a better visual display of the differences between these calculations and the results from reference 2. The integration method used to calculate these results began with initial conditions at about 38 km. This method of integrating from lower to higher altitudes was done so that the gap between about 130 to 100 km was not bridged. (Too much noise in the accelerometry would possibly influence lower atmosphere calculations.) The starting pressure was initially selected based on earlier calculations and iterated until the temperature appeared to merge with the temperature deduced from the mass spectrometry, about 120 K at 130 km. The effect of small errors in initial pressure is not observable in the temperature results at low altitudes since the pressure was relatively large. However, since a pressure error in the initial conditions propagates linearly upon integration of the barometric equation, large temperature errors were expected for altitudes where pressure is small. In this procedure, though, this error was readily removed by iteration, but only to the extent that pressure was known at the higher altitudes.

There are no major differences at lower altitudes in the general trend of the temperature profile determined in the present investigation compared with that of reference 2. This is not surprising since the flight-derived aerodynamic drag coefficients agree quite well with wind-tunnel drag as discussed. However, in the region above 70 km where significant differences in aerodynamics exist, the temperature determined by the flight-derived coefficients differs. That is, a temperature waviness more symmetric than earlier estimates was produced. The flight-derived coefficients produced two distinct major temperature bulges (temperature inversions) at 64 and 84 km which are of about equal magnitude and are preceded by two minor inversions at about 47 and 77 km.

Solving for the aerodynamic coefficients by using stagnation-pressure and mass-spectrometer data with accelerometer data allows for a unique method for determining the atmospheric structure. Use of the Viking lander capsule flight-derived coefficients in regions beyond current ground tests produced a warmer temperature profile merging into the mass-spectrometer data. However, the general trend of the existing temperature profile is not substantially changed (i.e., a waviness superimposed on a near-isothermal sructure). Thus, the existing complex atmospheric structure is not an artifact of the aerodynamics nor is it a product of the data processing methods.

CONCLUSIONS

Estimates of the Viking lander capsule aeroshell aerodynamic-force coefficients from the hypersonic-continuum-flow to the free-molecule-flow regimes have been obtained through techniques that made use of the onboard accelerometer, pressure, and mass-spectrometer data. The stagnation-pressure and acceleration

measurements combined with a calculation of the pressure coefficient were used to determine the hypersonic-continuum-flow aerodynamic-force coefficients.

The flight-derived drag coefficients agreed within 2 percent of ground-test estimates obtained from ballistic-range tests in CO_2 and wind-tunnel tests in CF_4 for Reynolds numbers greater than 1×10^5. A decrease in the ballistic-range drag coefficient between Reynolds numbers of 10^5 and 10^3 caused a difference between flight-derived and ground-test values in this range of 8 percent.

The free-molecule-flow drag coefficient was determined by a combined analysis of the mass-spectrometer and accelerometer data (imposing a density continuity constraint between them) and theoretical calculations using the theory of Hurlbut and Sherman. The values obtained ranged from 2.50 to 2.70 and were higher than the classical theoretical value of 2.20. No atmospheric measurements were obtained in the slip-flow region (between 85 and 135 km) and experimental sphere data were used to define the drag variation between the hypersonic-continuum-flow and the free-molecule-flow regimes.

The techniques used in the determination of the Viking lander capsule aeroshell aerodynamic-force coefficients were unique in that they could potentially be used to determine atmospheric sructure without the use of ground-test aerodynamic data. Application of the Viking lander flight-derived aerodynamic coefficients produced atmospheric temperature profiles of Mars similar to previous estimates for the regions where flight aerodynamic data and wind-tunnel data agree. Use of the flight-derived coefficients in regions beyond current wind-tunnel test conditions produced temperatures different than earlier estimates (most notably, warmer temperatures merging into the mass-spectrometer data). However, the general trend of the existing temperature-profile data was not substantially changed (i.e., a waviness superimposed on a near isothermal structure).

Langley Research Center
National Aeronautics and Space Administration
Hampton, VA 23665
November 25, 1980

APPENDIX A

ANALYSIS OF THE FLIGHT ACCELEROMETER AND GYRO DATA

The principal type of data for extracting information from the high-altitude portion of entry flight is acceleration data. A complete record of its main component, axial acceleration, is shown in figure A1 wherein the effects of the three decelerating systems mentioned previously are observed. On the Viking lander capsule, the accelerometers were incorporated into an inertial package with a triad of gyros whose input axes were aligned with the vehicle's body axis depicted previously. The accelerometer sensors measured a change in velocity in a fixed time interval produced by external forces such as aerodynamics or thrusters. Data were observed in quantized velocity increments of 0.0127 m/s for the axial channel and 0.00317 m/s for the normal and lateral channels. The different resolutions in the nonaxial channels were purposely designed to account for the relatively small size of the aerodynamic forces anticipated for a roll-controlled, conical, symmetrical body flying at a low angle of attack. The sampling rate was 10 samples per second on each channel with an internal up-down 10-bit register. However, the internal electronic data-transfer package was designed to preserve information internal to the inertial package. That is, sensor acquisition was not inhibited during transfer of data to the output devices. The accelerometers themselves were navigation-quality-type sensors with an expected scale factor of about 0.02 percent and a bias uncertainty of about 100×10^{-6} g_E.

There are several steps in preparing the acceleration flight-data records for aerodynamic analysis and interpretation. Since interest lies in a region with low signal, it is important to briefly review the major steps in this process. Attention will focus on the axial channel since this was the principal signal, although the process to be described is applicable to the other two data channels. The chief goal was to produce instantaneous center-of-gravity acceleration records due to aerodynamic forces only. The preliminary step in achieving this was to provide "raw" acceleration records by dividing the change in velocity output by 0.1 s after removal of signal transmission "blunder" points. This scaling process provides average acceleration over 0.1 s. (The quantized pulses were internally summed over 0.02-s intervals before being transmitted.) A time-smoothing process was then applied to these averaged data which consisted of fitting, in a least-squares method, a variable data length moving polynomial. This scheme was selected because of the following advantages: It provided a statistical average accounting for the measurement data noise; it accounted for averaging the internal acceleration buildup below the quantization level; and it tended to average the spurious periodic component of angular acceleration induced by accelerometer oscillations about the center of gravity. The major items to be selected with this preprocessing scheme are the length of interval of data to be averaged and the order of the polynomial to be used. It was found experimentally that a cubic polynomial with a variable-length data interval ranging from 100 points for a low acceleration reading to 10 points at maximum acceleration produced satisfactory results, that is, small deviations between the resultant cubic and the data.

APPENDIX A

Three problems were addressed before an accurate aerodynamics-induced acceleration record could be produced from the raw data. These consisted of removal of the bias, removal of the control-jet thruster-induced acceleration, and removal of the nonperiodic component of angular induced acceleration. The first problem, bias removal, was first solved by the Viking navigation entry team for the purpose of updating the onboard navigator prior to entry. Inflight data were collected by this team prior to the deorbit maneuver. These data were carefully analyzed and provided calibration values which were ultimately transmitted to the onboard computer to replace previously stored constants. The value obtained for the axial accelerometer was 0.01142 m/s^2 (0.03748 ft/s^2). To obtain assurance that this value did not change appreciably after deorbit, the accelerometer biases were recalculated for a quiescent period of time of 60 s just prior to observing the effect of the atmosphere. Figure A2 is a graph of the results of these calculations. Passing both a 200-point and 100-point moving cubic through the data produced biases of 0.00952 m/s^2 (0.03124 ft/s^2) and 0.00950 m/s^2 (0.03118 ft/s^2). These bias values were obtained by a linear regression analysis of the smoothed acceleration points produced by the method previously described. No detectable secular term appeared in the linear fit, lending some credence to the calculations. The bias test indicated that the bias was somewhat smaller (by about 200×10^{-6} g_E) and somewhat of a larger difference than anticipated since a bias calibration during interplanetary cruise produced only a 20×10^{-6} g_E difference with the aforementioned navigation-entry-team calculations. Although the results of the study indicated rather large bias-estimate differences and no appreciable changes in the value, the significance was in obtaining realistic error estimates of the final results. For example, the smallest of the deviations in the bias estimate was about 180×10^{-6} g_E. The approximate altitude at which the acceleration reaches this value was about 103 km; at this position, the measurement-bias uncertainty is about equal to the reading. Consequently, it was expected that large bias errors would result in application of these data at this altitude and above.

The second problem to be considered was the removal of the control-jet thruster-induced acceleration. This was a difficulty only for the axial channel since nominally the pitch- and yaw-vector thrusts are orthogonal to the plane of both the lateral and normal accelerometer-input axes whereas the roll thrusters were completely coupled. Figure A3 is a schematic of the locations of the RCS thrusters with respect to the lander body-axis system defined by X_b, Y_b, and Z_b, where positive X_b is directed toward the nose-cone heat shield. The appropriate location of the IRU, which contained the accelerometer triad, is also shown in this figure. The system of thrusters was completely redundant for mission safety and required firings in pairs to produce pitch-rate q or yaw-rate r angular motion. Roll-rate angular motions p were induced by comparable simultaneous pulse firings of coupled pairs of roll thrusters.

As seen in the figure, the direction of the thrust is such that it is opposite to the aerodynamic axial force. Thus, one would consistently underestimate the axial aerodynamic force if the thrust information were not removed. The information transmitted in the telemetry link to aid in the removal of the thrust from the axial accelerometer records included the cumulative number of commands issued to the pitch- and yaw-thruster pairs over each 0.2-s interval.

APPENDIX A

Using nominal vehicle mass and thruster performance gave an induced velocity increment of 0.000622 m/s (0.002040 ft/s) for each command to the thruster system. Thus, it would take approximately 20 cumulative commands before an unwanted quantum pulse would register in the X-accelerometer. It turned out that the thrust-induced acceleration had compensating features over the entry-flight regime. That is, during very low acceleration readings the thrusters were not fired very much to control the vehicle's attitude, whereas during higher acceleration inputs the thrusters were more active. Therefore, there was a fairly small, constant-percentage-level error induced by the thrusters. Effort was expended to remove this error input into the X-accelerometer by applying corrections obtained from the telemetered command information.

The last problem to be addressed regarding nonaerodynamic inputs into the accelerometer was the contribution due to angular accelerations of the accelerometer package about the vehicle center of gravity. Practicality in spacecraft design prohibited mounting the IRU at the vehicle center of gravity. In general, the correction for angular-acceleration inputs can be expressed as the following transformation:

$$\vec{\Delta A} = -\dot{\Omega}\vec{X} \tag{A1}$$

where Ω is a 3 by 3 matrix composed of squares of angular rates and angular-acceleration terms of the vehicle about the center of gravity and $\vec{X}$ is the vector location of the accelerometer with respect to the center of gravity. For the Viking Lander 1 $\vec{X}$ = (0.10196 m, 0.27719 m, -1.01140 m). Thus, to obtain center-of-gravity accelerations along the body axis, $\vec{A}_b$ required the following vector addition:

$$\vec{A}_b = \vec{A}_m + \vec{\Delta A} \tag{A2}$$

where $\vec{A}_m$ is the measured acceleration at location $\vec{X}$.

The correction component for the measured axial acceleration is written explicity as

$$\Delta A_x = 0.10196(q^2 + r^2) - 0.27719(pq - \dot{r}) + 1.01140(pr + \dot{q}) \tag{A3}$$

To obtain a semiquantitative insight into the nature of this correction, assume momentarily that pitch motion is predominant, that is, $r = p = 0$. Therefore,

$$\Delta A_x = 0.10196q^2 + 1.01140\dot{q} \tag{A4}$$

Note that the second term is about 10 times larger than the first term due to lever-arm differences. Furthermore, since in general we are dealing with

small rates, the square of q additionally contributes to making the second term larger than 10 times the first term. Fortunately $\dot{q}$ is cyclic and, as explained earlier, the smoothing process tends to average out cyclic inputs into the accelerometer.

This simple example, although instructive, is not the entire picture since, as one might imagine from figure A3, a pitch maneuver practically always was accompanied by a yaw motion due to small differences in thrust level and thruster-alignment irregularities. Hence, the complete magnitude of this spurious input is complex and requires additional examination of the angular body motions of the lander.

The Viking lander gyros were strap-down, navigation-type quality sensors which required similar preprocessing as the accelerometers. Their quantized output measured the incremental angular change in the vehicle attitude about three body axes in a fixed interval of 0.1 s. The Viking Lander 1 level of quantization for each axis was

$$\left.\begin{aligned} \Delta\theta_q &= 7.9036 \times 10^{-4} \text{ deg} \\ \Delta\theta_r &= 7.9261 \times 10^{-4} \text{ deg} \\ \Delta\theta_p &= 8.0042 \times 10^{-4} \text{ deg} \end{aligned}\right\} \tag{A5}$$

where the direction in angular change is indicated by the subscripts q, r, and p and the corresponding rotational axes are shown in figure A3. In general, the approximate resolution level for rates about the three body axes was about 10 times the quantization level, or 0.008 deg/s. An inflight bias calibration for the gyros was also performed by members of the navigation flight team. This provided the following results:

$$\left.\begin{aligned} q_b &= -1.58325 \times 10^{-3} \text{ deg/s} \\ r_b &= -2.4864 \times 10^{-3} \text{ deg/s} \\ p_b &= -1.7923 \times 10^{-3} \text{ deg/s} \end{aligned}\right\} \tag{A6}$$

To date, no attempt has been made to verify these bias calculations as was done with the accelerometer data. The polynomial smoothing process described earlier for the accelerometer data was applied to the gyro flight data with a great deal of success. An additional step was taken to provide insight into the angular acceleration components (i.e., $\dot{q}$, $\dot{r}$, and $\dot{p}$) by differentiating the resulting smooth rate curves in order to calculate $\Delta\vec{A}$.

APPENDIX A

To conveniently examine the spurious inputs into the axial channel, the correction term for the measured axial acceleration (that is, eq. (A2)) can be separated into two parts. The nonperiodic term can be written as

$$\Delta A_{x,se} = 0.10196(q^2 + r^2) - 0.27719pq + 1.01140pr \tag{A7}$$

whereas the periodic term is

$$\Delta A_{x,per} = 0.27719\dot{r} + 1.01140\dot{q} \tag{A8}$$

After the aforementioned preprocessing of the gyro, the magnitude of each of the components of the angular acceleration into the axial accelerometer was calculated. The results are shown in figure A4. The expected nonperiodic nature and complexity of the correction term $\Delta A_{x,se}$ is displayed in the upper graph of this figure. These mostly positive values would accumulate in the accelerometer system to yield an underestimate of the true acceleration if not taken into account. This underestimate of acceleration would produce an underestimate in aerodynamic coefficient. Fortunately, on the average, this contribution was very small, much less than 5×10^{-5} m/s^2. A constant spurious acceleration of 5×10^{-5} m/s^2 would require over 250 s to produce one pulse. This is too long to be of importance when compared with the time scale of the entry.

The lower graph in figure A4 (labled $\Delta A_{x,per}$) displays the expected periodic contribution to the axial channel. As discussed in the previous semiquantitative argument, this term was much larger than the nonperiodic component. Here, for instance, a constant acceleration of 7×10^{-3} m/s^2 would require only about 1.8 s to introduce a pulse. But because of the periodic nature of this component, alternate pulsing would take place which was readily removed by most smoothing schemes of a few seconds length. Thus, over the hypersonic-continuum-flow flight regime, the location of the Viking lander accelerometer with respect to the vehicle center of gravity was not a significant error source and was accounted for by the application of the smoothing process.

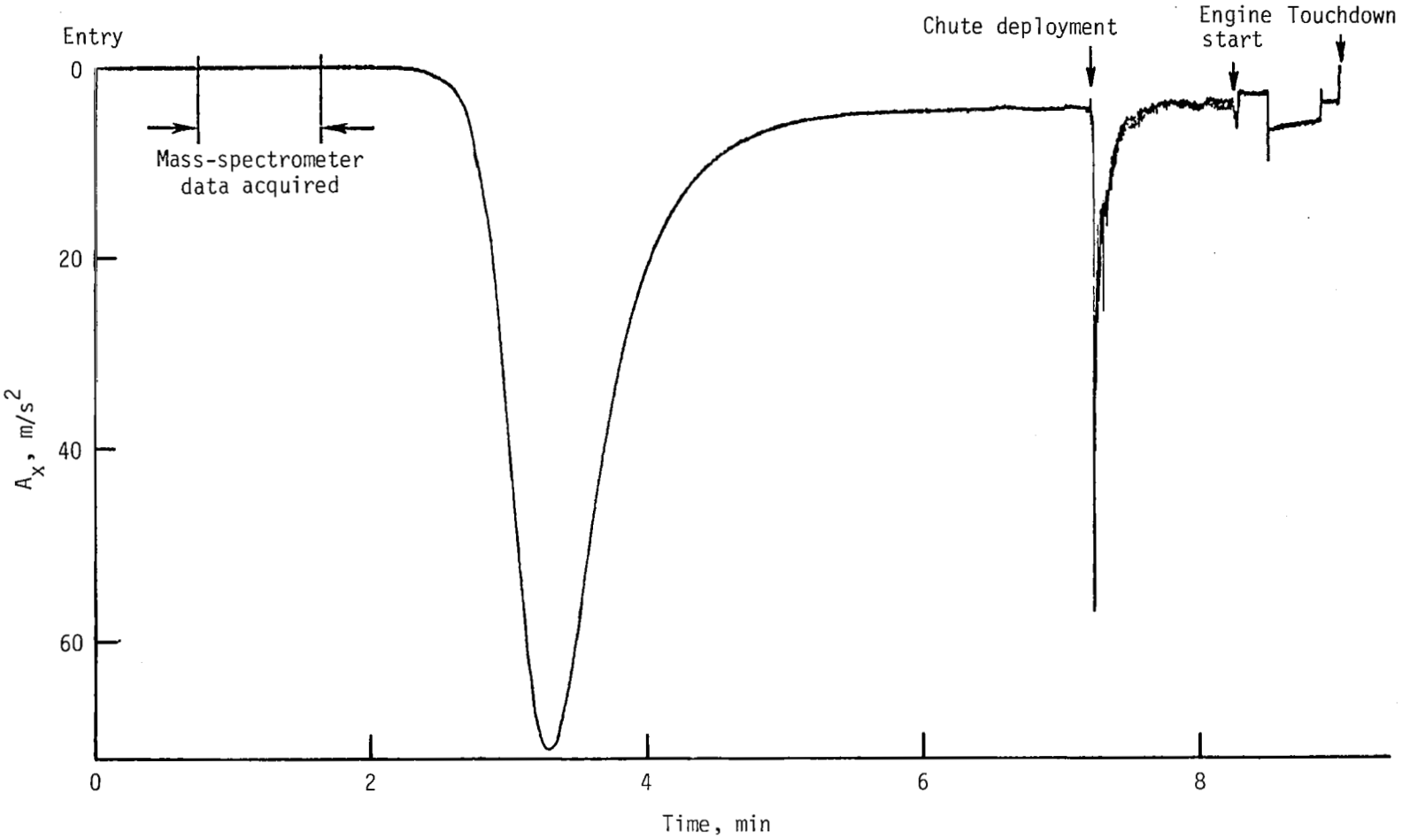

Figure A1.- Viking Lander Capsule 1 axial-acceleration data.

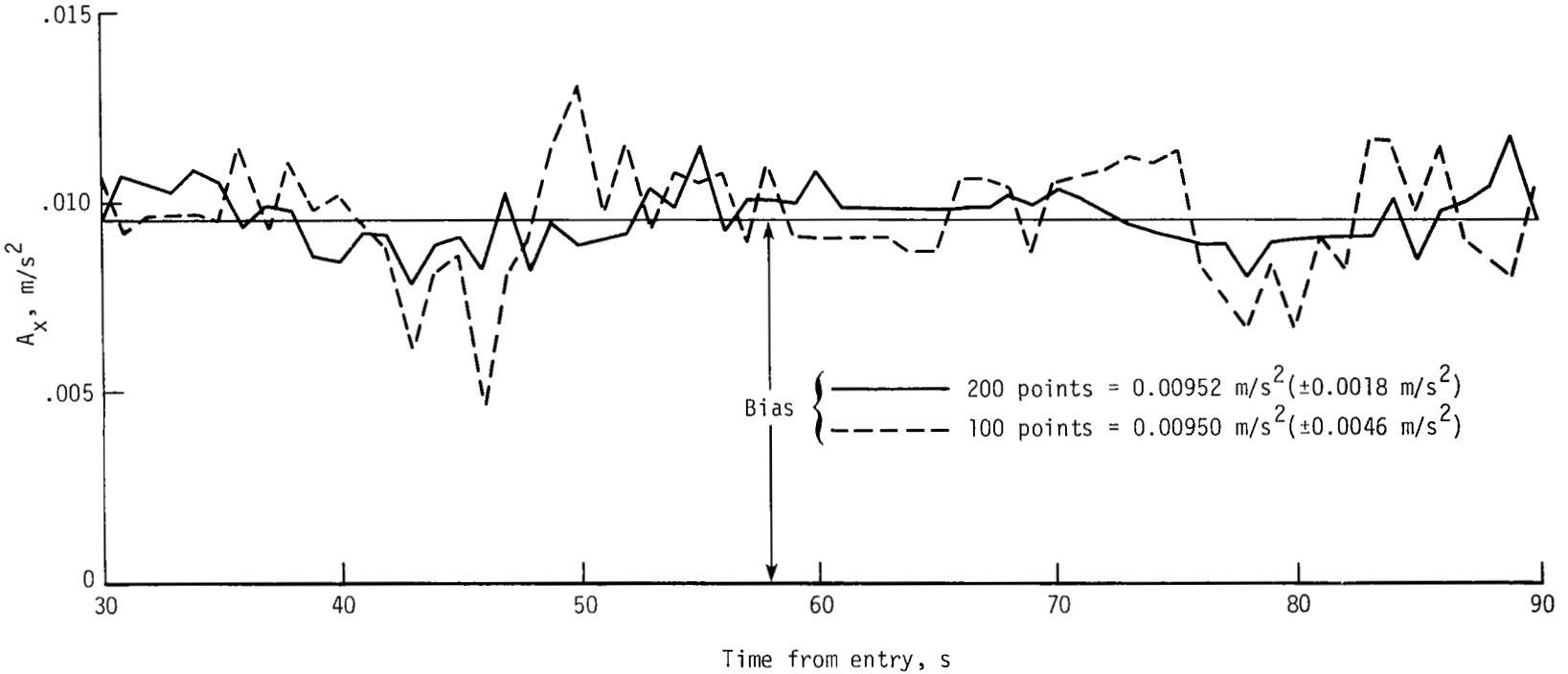

Figure A2.- Viking Lander Capsule 1 axial-acceleration bias calculation.

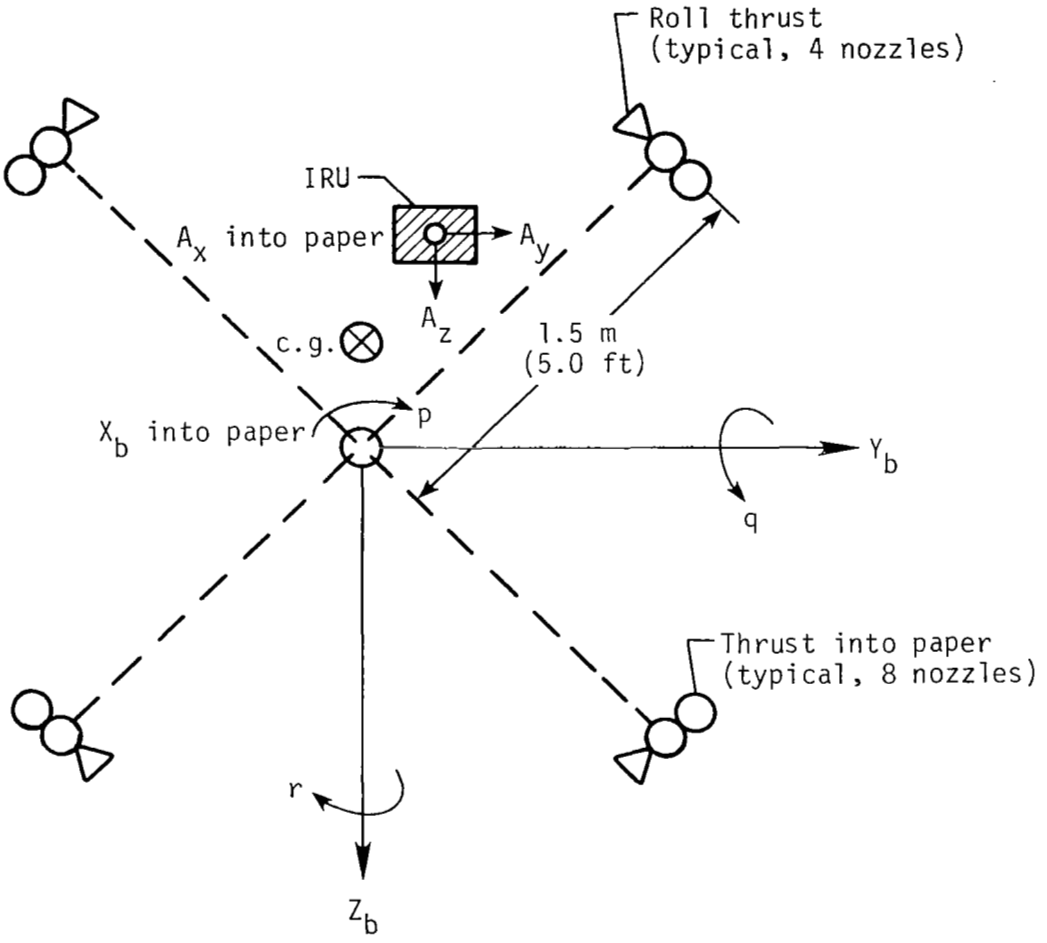

Figure A3.- Locations of RCS thrusters and IRU with respect to vehicle body axis.

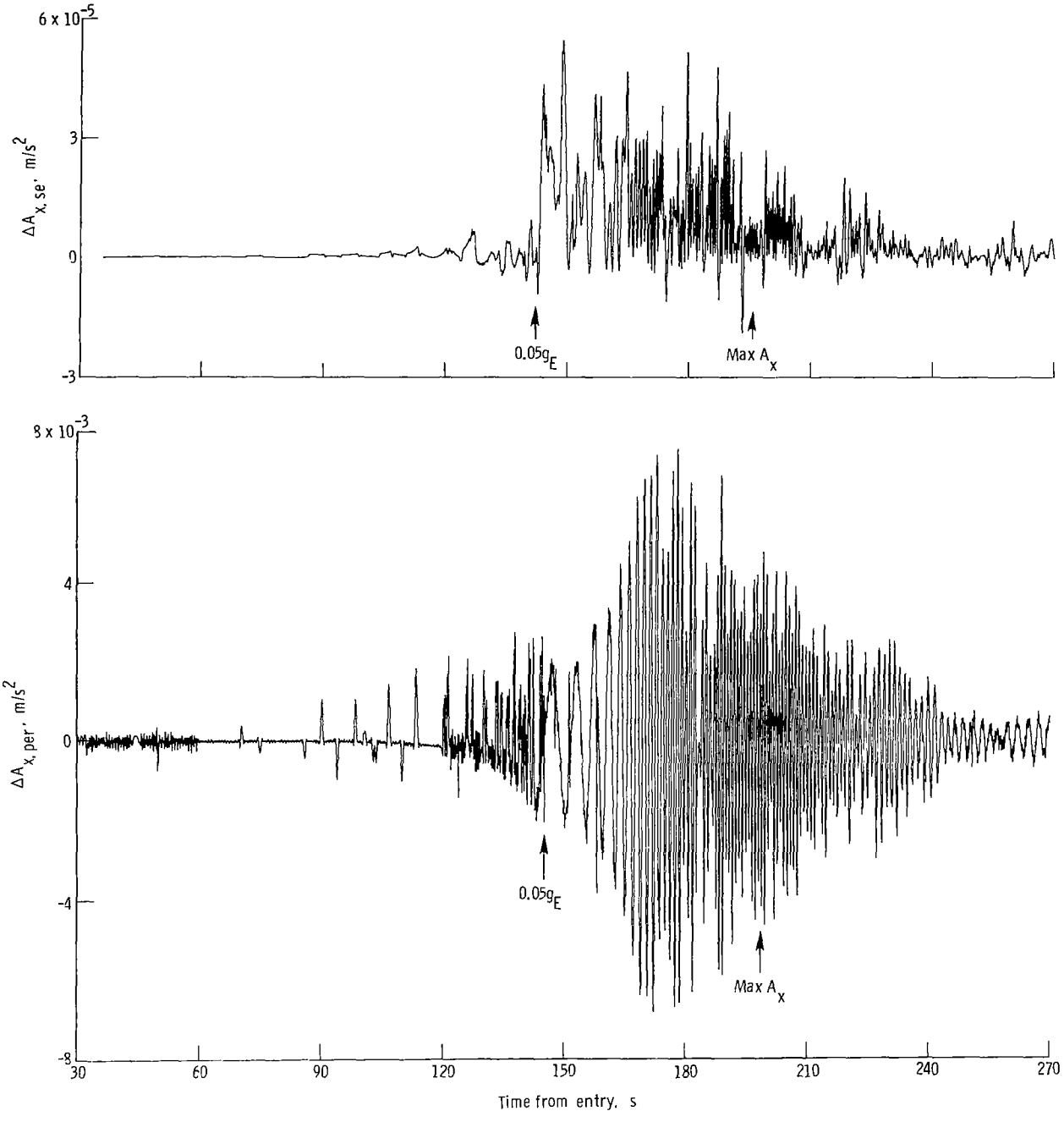

Figure A4.- Correction components of angular acceleration into axial accelerometer calculated from gyro data.

APPENDIX B

ANALYSIS OF PRESSURE DATA

The location on the aeroshell of the pressure sensor used in the following analysis is shown in figure 2 as the stagnation-pressure sensor. When the vehicle was pitched down to its trim flying condition, the sensor orifice was very near the stagnation point. A description of the instrument and its development and laboratory calibrations have been reported in detail in reference 21. Several pertinent areas of the instrument's capabilities will be briefly reviewed here for completeness.

This sensor measured pressures by changes in capacitance produced by deflection of a thin stretched stainless-steel diaphragm referenced to a vacuum chamber behind it. The electronics were arranged so that this unit had two output ranges nominally, 0 to 150 millibars and 0 to 20 millibars. Quantized samples were taken every 0.2 s over the region of interest with an 8-bit telemetry-word producing nominal pressure-data resolutions of about 0.60 and 0.08 millibar over the two ranges. Actual subsystem electronics design on the full-range scale gave a resolution nearer to 0.81 millibar, whereas the smaller range was nearer to 0.15 millibar. The actual collection of stagnation-pressure-sensor data over the two ranges is shown in figure B1. After calibration data from reference 21 were applied to the measurements, they were corrected by removing the end-to-end zero-shift caused by a combination of sensor effects, such as output design sensitivity and minute changes in diaphragm spacing, and measurement effects, such as rarefied orifice flow. Removal of the zero-shift (bias) was accomplished by examining the data just prior to sensing appreciable atmosphere as defined by the acceleration data. Figure B2 shows the results of the brief study to remove the zero-shift. The results are:

High-range zero-shift = 1.2454 millibars

Low-range zero-shift = 1.3117 millibars

To further prepare the pressure data before combining with the accelerometer data, the smoothing technique described previously was also applied. A second-order polynomial was adequate for smoothing the pressure data. During the high-altitude flight regime (above about 50 km) the low-range pressure data were used in the aerodynamic calculations. At 50 km, the low-range channel saturated and high-range data were used with a relatively smooth transition occurring between the two ranges.

The telemetry resolution of the low-range pressure data limited the altitude for meaningful aerodynamic calculations. Figure B3 is a graph of part of the smoothed low-range pressure data in terms of data-resolution elements (1 element = 0.15 millibar). Also included are the corresponding altitudes from the trajectory-reconstruction process. At about 135 s from the entry point, the measured level of pressure is equal to the telemetry resolution, which can be interpreted as a 100-percent error in the measured pressure,

whereas at 150 s the error is about 10 percent. This manner of interpreting measurement error is conservative since the smoothing process provided formal statistics which are somewhat smaller than those implied by this figure, particularly during times when pressure was not changing rapidly. (That is, the same level measured repeatedly produced a better estimate of the average.) A rough order estimate of pressure-measurement errors introduced into the subsequent aerodynamic calculations was obtained from this analysis. For example, figure B3 indicates that the errors introduced by pressure-measurement uncertainty would be larger than about 25 percent above an altitude of about 76 km. This relationship between pressure-measurement errors and altitude is important for limiting the aerodynamic calculations since an erroneous interpretation could occur. This happens because the limits of the pressure measurement are near the onset of the slip-flow regime and calculations with this inaccurate data produce aerodynamic variations similar to what is expected when moving into the slip-flow regime.

Correction of the pressure data to account for low-density "orifice effects" was carried out by using the semiempirical theory presented by Potter et al. (ref. 22) and extended by Guy and Winebarger (ref. 23). According to these references, the pressure measured under low-density-flow conditions is influenced by local flow conditions and the aerodynamic heating rate in the vicinity of the pressure orifice. Application of the orifice-effects correction theory using Viking conditions resulted in a pressure correction of at most about 3 percent of the measured value at about 76 km. Thus, this effect on the measurement error was considered negligible compared with the telemetry-resolution errors mentioned previously. Various other rarefied-flow effects, such as viscous effects, orifice-tube time lag, and momentum mixing, were considered but found to be insignificant at the altitude at which the pressure data were usable, that is, below 84 km as shown in figure B3.

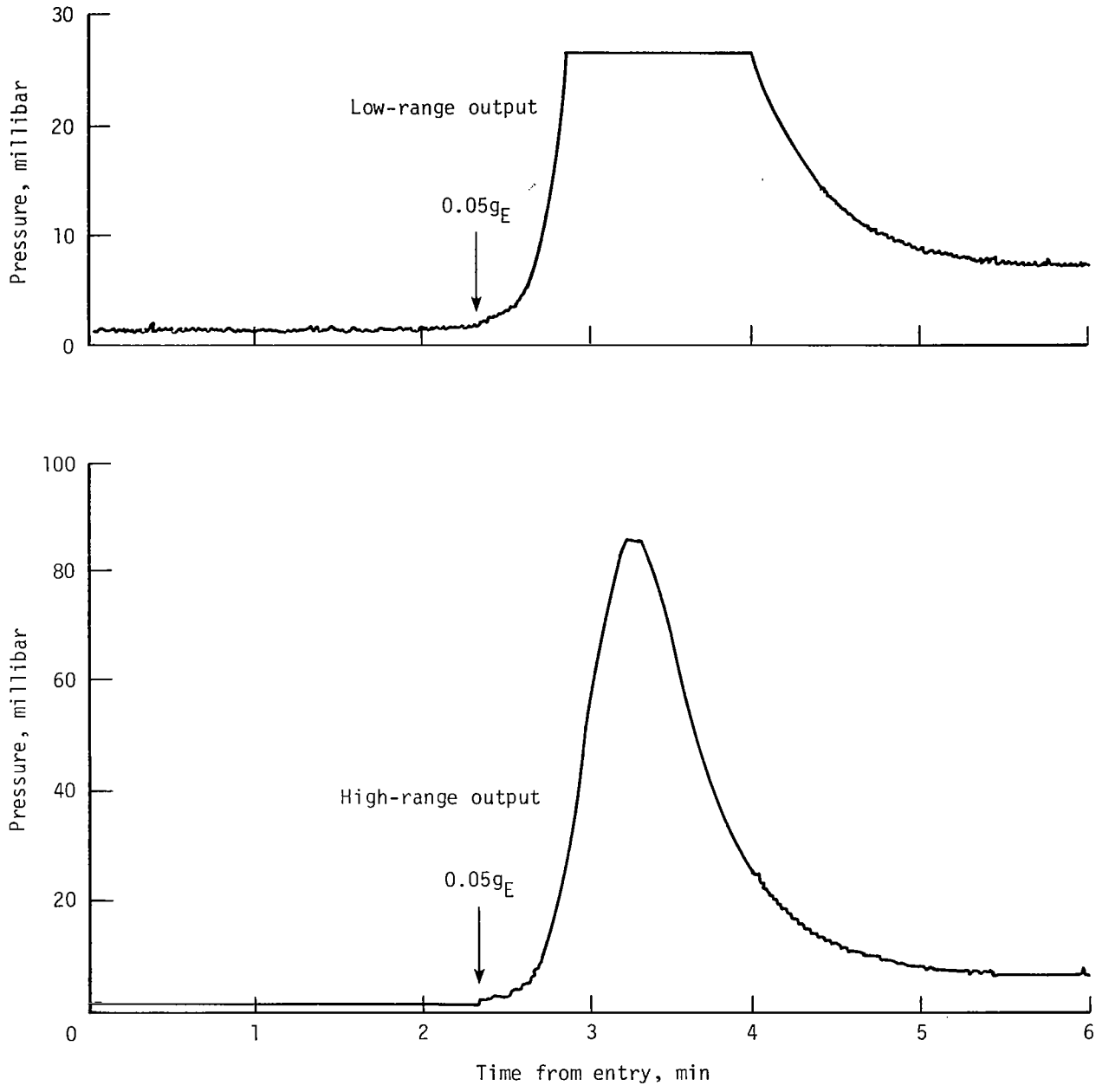

Figure B1.- Viking Lander Capsule 1 stagnation-pressure data record.

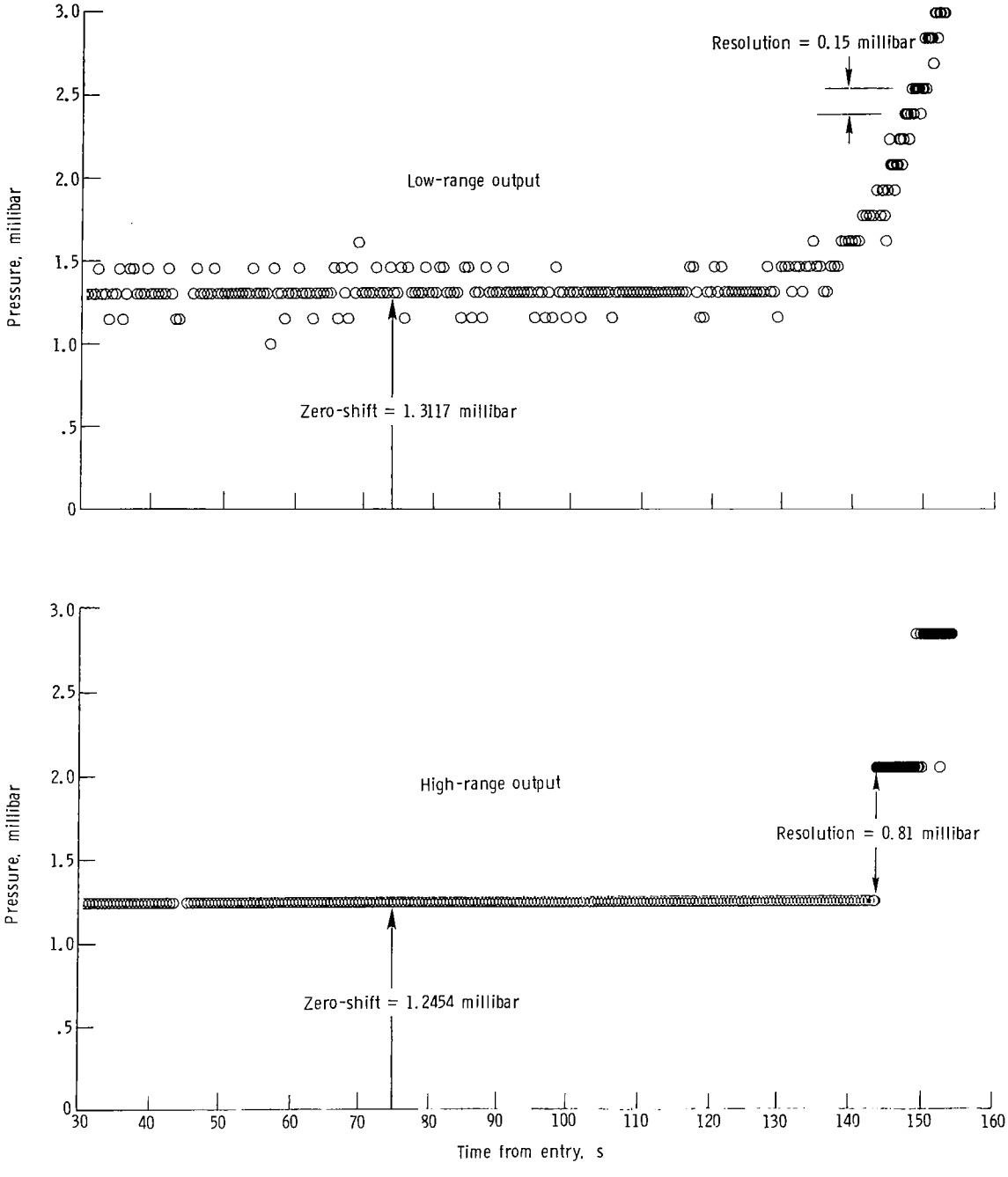

Figure B2.- Estimation of stagnation-pressure zero-shift.

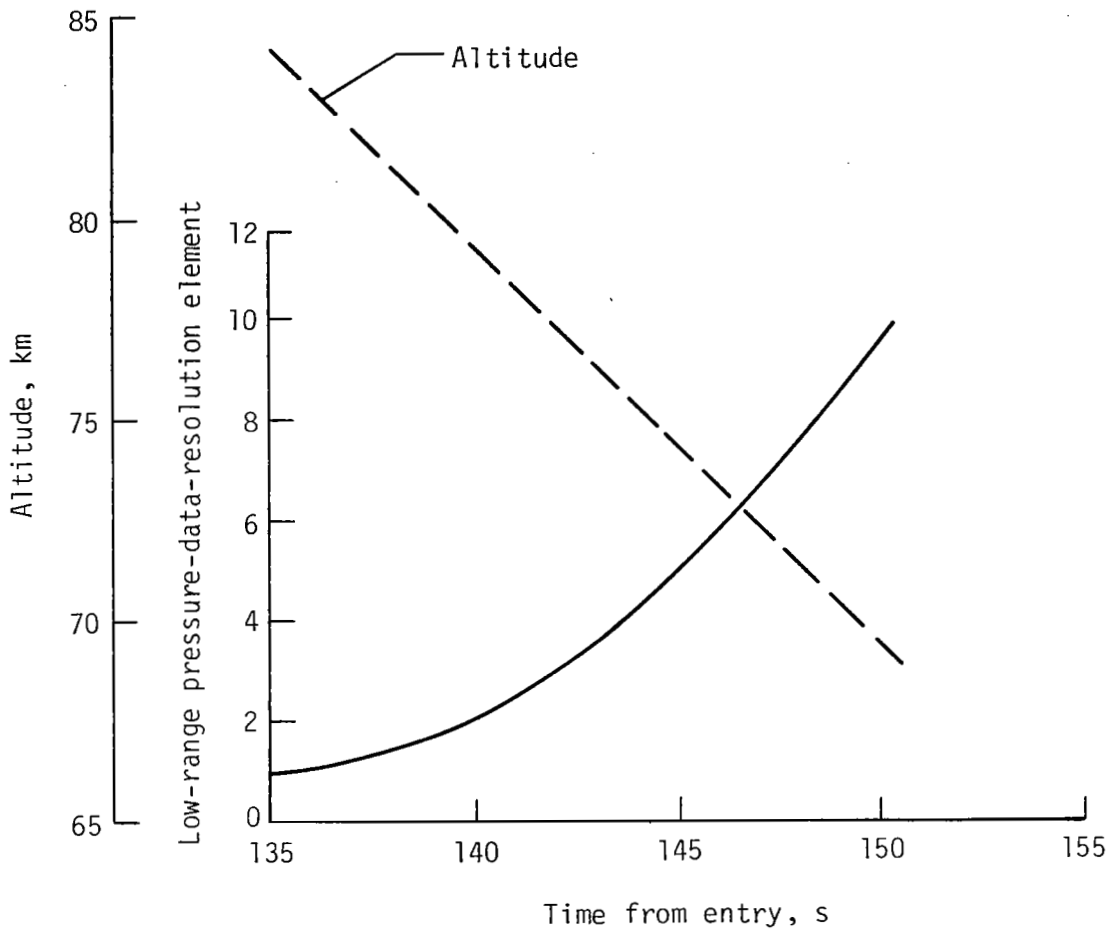

Figure B3.- Relationship of low-range pressure resolution and altitude.

APPENDIX C

ANALYSIS OF MASS-SPECTROMETER DATA

The last major data prepared for analysis was that taken by the Viking lander upper atmosphere mass spectrometer (UAMS). Figure 2 shows the relative location of this instrument on the aeroshell, which is flush-mounted to the surface with a 4.45-cm (1.75-in.) orifice to the gas stream. This experiment (ref. 1) provided quantitative in situ data on the neutral composition of the upper atmosphere of Mars. The description of the open-source, double-focusing instrument, the calibration technique, and expected data quality are documented in reference 24. For the application of these data to the experiment described herein, pertinent features of the data acquisition and preparation required to obtain atmospheric mass density will be briefly reviewed.

The acquisition period of the mass spectrometer data is shown in conjunction with the accelerometer data in figure A1. For the period of time corresponding to the altitude range of 200 km to about 125 km, the vehicle attitude was at an angle of attack of about -11.1°. This vehicle attitude was held nearly constant by the onboard navigation system as mentioned previously. The data from the first entry, which provided altitude profiles of number densities of four major constituents - CO_2, N_2, A_r, and O_2 - have been reported in reference 12. The preparation task of this experiment was to convert these data to total mass density. This was accomplished for each altitude with the following calculations:

$$\left.\begin{aligned} n_t &= n(O_2) + n(Ar) + n(CO_2) + n(N_2) \\ \mathcal{M} &= \left[32n(O_2) + 40n(Ar) + 28n(N_2) + 44n(CO_2)\right]/n_t \\ \rho &= \frac{\mathcal{M} n_t}{N_o} \end{aligned}\right\} \qquad (C1)$$

where n(species) is the measured number density of that species. The mean molecular weight $\mathcal{M}$ was calculated separately to obtain total atmospheric pressure and temperature. The expected overall accuracy of the instrument was on the order of 10 percent. As reported in reference 3, the calculation of total mass density incurred additional errors when minor species, and particularly the reactive species atomic oxygen, were neglected. This type of error became progressively more severe as altitude increased. However, as seen in the "Analysis of Flight Data" section, the particular application of these data dealt with altitudes below approximately 150 km. Consequently, the error induced by not including the minor species was believed to be less than the level of accuracy of the calibrated instrument output. For example, Hanson's interpretation of the RPA data (ref. 25) yielded an atomic-oxygen number density of 5×10^8 molecules per cubic centimeter at an altitude of 135 km which contributed about

0.013×10^{-12} g/cm^3 to the total mass density. At this altitude, the major atmospheric constituents contributed about 2.0×10^{-12} g/cm^3. Thus, neglecting the contribution of atomic oxygen produced less than a 1-percent error in the mass-density calculation. In essence, neglecting the contributions of minor species caused an underestimation of total mass density, which produced an overestimate of drag coefficient for a given acceleration. Table I is a summary of the results of these calculations.

TABLE I.- MASS-SPECTROMETER/MASS-DENSITY DATA

Altitude, km	Mean molecular weight, g/g-mol	Mass density, g/cm^3
128.0	43.61	5.83×10^{-12}
134.0	43.40	1.97×10^{-12}
139.5	43.21	8.40×10^{-13}
145.5	43.06	4.46×10^{-13}
151.0	42.78	2.34×10^{-13}
163.0	42.32	7.96×10^{-14}
175.5	41.97	2.92×10^{-14}
182.0	41.86	1.55×10^{-14}
187.5	41.22	8.11×10^{-15}
194.0	40.06	4.40×10^{-15}
199.5	38.67	2.31×10^{-15}

APPENDIX D

REVIEW AND APPLICATION OF FREE-MOLECULE-FLOW MODEL

In spite of the fact that free molecule flow has been the subject of intensive study, the determination of free-molecule-flow drag coefficients is still subject to considerable uncertainty. The classical approach, as exemplified by Schaaf and Chambre (ref. 26), basically summarizes the aerodynamic-force calculations for the two limiting types of gas-molecule surface interactions: (1) A specular reflection for which the velocity component normal to the surface is reversed and the tangential component of momentum of the molecules is unchanged, and (2) a diffuse reemission of molecules having a Maxwellian velocity distribution corresponding to some mean reference temperature T_{ref}. In this classical approach, the surface interaction is typified by three empirical constants α, σ, and σ'. Of these three constants, the best known is the accommodation coefficient α, which represents the degree to which the incident molecules are accommodated to the surface temperature, that is,

$$E_{ref} = E_i + \alpha(E_w - E_i) \tag{D1}$$

where E_w is the energy flux the reflected molecules would have if they had a Maxwellian distribution corresponding to T_w. The second constant σ may be interpreted as the fraction of the incident molecules that are temporarily absorbed and then reemitted diffusely (or, alternately, the incident-molecule tangential-momentum transfer fraction). The third constant σ' relates the normal pressure (or normal momentum) on the surface due to reemitted molecules P_{ref} to the pressure on the surface from incident molecules P_i in a manner analogous to the accommodation equation, that is,

$$P_{ref} = P_i + \sigma'(P_w - P_i) \tag{D2}$$

where P_w denotes a fictitious pressure which would be exerted on the surface if the molecules were reemitted diffusely with a mean temperature equal to T_w. Experimental evaluation of these constants for various surface-material gas-molecule combinations has proven to be exceedingly difficult. In recent years, there has been a growing awareness that this classical model cannot adequately describe the actual molecule-surface interactions. Accordingly, free-molecule-flow theories have been developed in which the molecule-surface interaction has the characteristics observed in molecular-beam experiments (refs. 27 and 28).

Schamberg (ref. 29) proposed a model in which the reflected molecules are contained in a conical beam of half-angle width ϕ, having a direction of reemission θ_{ref} measured from the vehicle surface to the axis of the reflected beam. The distribution of particles within the beam is taken to be a cosine

distribution, that is,

$$N_{ref}(\Phi) = K \cos\left(\frac{\pi\Phi}{2\phi}\right) \tag{D3}$$

where N_{ref} is the number of reemitted molecules per unit time whose directions of reemission relative to the beam axis lie between Φ and $\Phi + d\Phi$. The term K is a proportionality constant dependent on the molecule reemission distribution model. In the Schamberg model, the molecule-surface interaction is described by the three parameters ϕ, ν, and α where ϕ is the half-angle of the reflected molecular beam width, ν relates the angle of reflection to the angle of incidence through the expression

$$\cos\theta_{ref} = (\cos\theta_i)^{\nu} \qquad (\nu \geq 1) \tag{D4}$$

and α is the accommodation coefficient, which relates the velocities of the reflected and incident molecules through the expression

$$\frac{V_{ref}}{V_i} = \sqrt{1 + \alpha\left(\frac{T_w}{T_i} - 1\right)} \tag{D5}$$

The incident molecules are assumed to approach the surface with a uniform incident velocity V_i which corresponds to a kinetic temperature T_i and along a direction defined by θ_i. The temperature T_i is related to the velocity V_i through the relationship

$$T_i = \frac{\mathcal{M}_i V_i^2}{3k} \tag{D6}$$

where $\mathcal{M}_i$ is the molecular weight. The reflected molecules are assumed to have a uniform reemission velocity V_{ref}.

Although the Schamberg model is in much better agreement with molecular-beam data than the classical model, the assumption of uniform reemission velocity for all directions is not realistic. Hurlbut and Sherman (ref. 14) replaced Schamberg's uniform velocity assumption with the Nocilla wall reflection model (ref. 15) which features a "drifting" Maxwellian distribution function for the reemitted molecules. Using experimental results as a guide, Hurlbut and Sherman assume a dependence of accommodation coefficient α_2, angle of reflection θ_{ref}, and reemitted molecule-speed ratio S_{ref} on the angle of incidence θ_i as shown in figure D1. Here, the accommodation coefficient α_2 is a "partial"

accommodation coefficient defined as

$$\alpha_2 = \frac{\varepsilon_i(\theta_i) - \varepsilon_{ref}}{\varepsilon_i(\theta_i) - \varepsilon_w} \tag{D7}$$

where ε_i is the mean energy of particles in the incident beam and ε_{ref} and ε_w are respectively the mean energies of the reflected molecules (taken over the entire distribution of velocities) and of gas particles scattered in a Maxwellian reemission from a wall at temperature T_w. The reemitted molecule-speed ratio S_{ref} is defined as,

$$S_{ref} = \frac{V_{ref}}{\sqrt{2RT_{ref}}} \tag{D8}$$

where V_{ref} is the macroscopic (or "drift") velocity. In Hurlbut and Sherman's analysis, the molecule-wall interaction can be defined by the two parameters $\alpha_{2,o}$ and $S_{ref,o}$. In the limiting cases of completely diffuse or specular reflection, both the Schamberg and the Hurlbut and Sherman analyses reduce to the classical result of Schaaf and Chambre for the values of the parameters in the following table:

	Parameter values for -		
Reflection	Schaaf and Chambre analysis	Schamberg analysis	Hurlbut and Sherman analysis
Specular	$\alpha = \sigma = \sigma' = 0$	$\nu = 1$ $\phi = 0$ $\alpha = 0$	$\alpha_{2,o} = 0$ $S_{ref,o} = \frac{V_\infty}{\sqrt{2RT_\infty}}$
Diffuse	$\alpha = \sigma = \sigma' = 1$	$\nu = \infty$ $\phi = \pi/2$ $\alpha = 1$	$\alpha_{2,o} = 1^*$ $S_{ref,o} = 0$

*For all θ_i.

All things considered, Hurlbut and Sherman's analysis appears to be one of the most realistic development models to date. Experience with both the Schamberg and the Hurlbut and Sherman models has shown that the assumed "width" of the reflected beam (as prescribed by ϕ or S_{ref}) has only a relatively small

(less than 20 percent) effect on the calculated drag coefficient. The angle of reflection θ_{ref} (prescribed by ν in the Schamberg model) can significantly influence the calculated drag coefficient but, based on experimental data, Hurlbut and Sherman assume $\theta_{ref} = \theta_i$. Hence, the major uncertainty involved in calculating a free-molecule-flow drag coefficient is associated with the selection of the accommodation coefficient. Although the literature contains many experimental measurements, obtained prior to 1960, that show accommodation coefficients close to 1, a careful survey of these data showed them to be untrustworthy (ref. 30). Subsequent studies have shown that a wide range of accommodation coefficients are possible depending on the gas-molecule surface combination under consideration, the cleanliness of the surface (presence of adsorbed gas molecules), the velocity and direction of the incident beam, and so forth. Because of the uncertainties associated with experimentally measured accommodation coefficients, several investigators have carried out theoretical analyses. Cook (ref. 31) discussed several theories and concluded that the true value for the accommodation coefficient probably lies between

$$\alpha = \frac{4\mu}{(1 + \mu)^2} \qquad (\mu \leq 1) \qquad \text{(D9)}$$

and

$$\alpha = \frac{2\mu}{(1 + \mu)^2} \qquad (\mu \geq 1) \qquad \text{(D10)}$$

where μ is the ratio of the mass of the incident gas molecule to that of a surface atom. Equation (D9) results from considering a head-on collision of incident molecules and surface atoms which are both smooth, hard spheres. Equation (D10) results from the theory of Baule (discussed in ref. 31), wherein the surface is represented by an oscillating cubic lattice, the energy transfer is determined by averaging over all angles of incidence, and a single collision between hard spheres is assumed.

Öpik (ref. 32) has also calculated average values of accommodation coefficients using the hard-sphere model. He made some allowance for the fact that all impacts are not head-on collisions and computed values that were slightly less than those given by equation (D9). Theoretical calculations by Oman et al. (refs. 33 and 34) and by Hurlbut (ref. 35) which involved realistic three-dimensional surface lattices, employed Lennard-Jones interaction potentials, and allowed for multiple collisions and various incidence angles have yielded values of α between those predicted with equations (D9) and (D10). Furthermore, these calculations showed that the mean value of the accommodation coefficient averaged over all directions θ_{ref} for a given angle of incidence θ_i was maximum for normal incidence and decreased to zero at grazing incidence. This is the basis for the α_2 variation assumed by Hurlbut and Sherman and shown in figure D1.

APPENDIX D

For the present application, the Viking lander capsule aeroshell was covered with thin aluminum sheeting and the Martian atmosphere was composed of about 97-percent CO_2 at the altitudes where the aeroshell experienced free molecule flow. Hence, the boundaries of μ can be approximated by

$$1.3 < \mu < 1.6 \tag{D11}$$

where the lower bound follows the suggestion of Cook that the outermost layer, assumed to be chemisorbed oxygen, should be used in the calculations of μ. In any event, the value of μ is greater than 1.0 and it is anticipated that the value of the accommodation coefficient is large. The formal limits of the accommodation coefficient at $\mu = 1.0$ from equations (D9) and (D10) are from 0.5 to 1.0. For $\mu > 1.0$ little data exists, since for most Earth applications this condition rarely exists. However, Öpik, Oman et al., and others suggest that for μ near 1.0, the bounds for the accommodation coefficient could be in the range

$$0.90 \leqq \alpha \leqq 1.0 \tag{D12}$$

although Oman et al. suggests that $\alpha = 1.0$ for $\mu >> 1$.

In light of the foregoing discussion, the free-molecule-flow theory of Hurlbut and Sherman with $\alpha_{2,o}$ ranging from 0.9 to 1.0 was used to predict the drag coefficient for the Viking lander capsule aeroshell. For the Viking lander capsule entry conditions the average value of the incident free-stream molecule-speed ratio is

$$S = \frac{V_\infty}{\sqrt{2RT_\infty}} \approx 19 \tag{D13}$$

Variations of S are about ±3 which, for these large values, do not significantly influence the calculations. In accordance with Hurlbut and Sherman, for $S > 10$,

$$S_{ref,o} = \frac{V_{ref}}{\sqrt{2RT_{ref}}} \equiv 10 \tag{D14}$$

and

$$\frac{RT_w}{V_\infty^2} \equiv 0.001 \tag{D15}$$

which corresponds to a wall temperature of about 110 K. This is approximately equal to the colder range of the atmospheric temperature which lies between 100 and 200 K. (Doubling the ratio value, which corresponds to the larger temperature value, affects the calculations by less than 1 percent.) The drag coefficient resulting from the calculations with the Hurlbut and Sherman theory is presented as a function of vehicle angle of attack in figure D2. Also shown for comparison purposes are the limiting case of completely specular reflection and the midrange value of the accommodation coefficient. As can be seen from figure D2, the range of drag coefficients calculated with the Hurlbut and Sherman model (using the parameter chosen in the preceding discussion) is 2.54 to 2.63 for the vehicle attitude, which is fixed by the onboard navigation system. Placed on the figure is the value obtained from the analysis with the accelerometer and mass-spectrometer data (i.e., $C_D = 2.55$). Clearly, this independent method produces a drag coefficient which is in the range of the anticipated values. However, the method used to obtain this flight value required interpolation and certain assumptions which may prove to be fortuitous. Consequently, conservative values ranging from 2.50 to 2.70 were chosen for the free-molecule-flow drag coefficient. These values are significantly higher than the value corresponding to the widely used classical diffuse limit of 2.20.

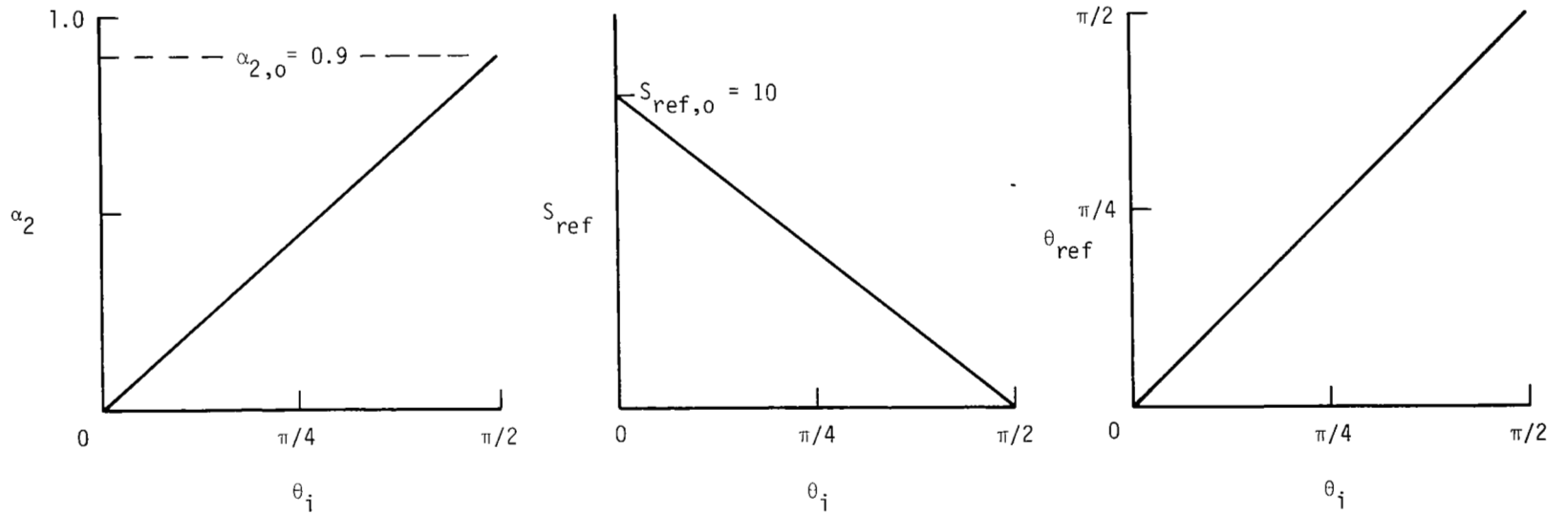

Figure D1.- Dependence on incidence angle θ_i of accommodation coefficient, speed ratio of reflected molecules, and angle of reflection θ_{ref} used in present investigation.

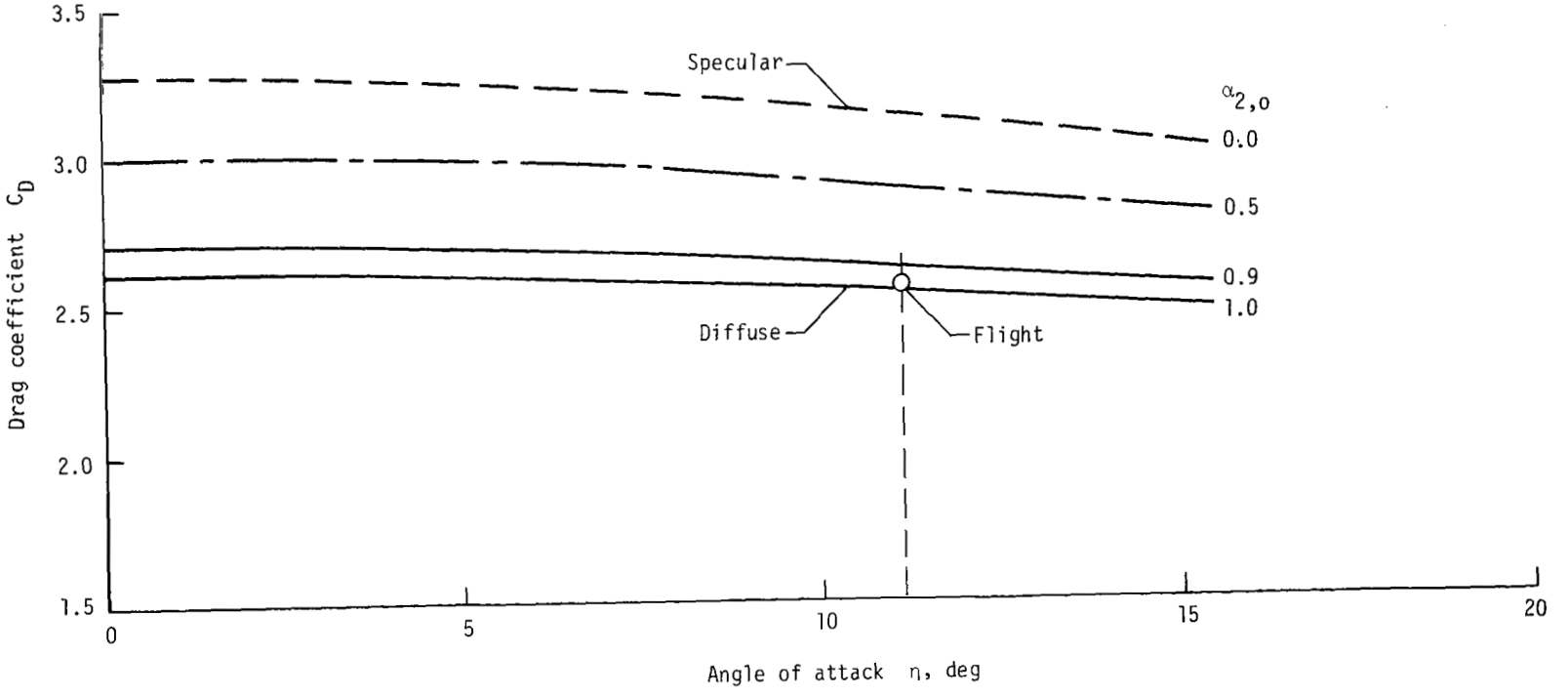

Figure D2.- Free-molecule-flow drag coefficient for Viking lander capsule from Hurlbut and Sherman theory. $RT_w/V_\infty^2 = 0.001$; $S_{ref,o} = 10$; $S = 19$.

REFERENCES

1. Nier, A. O.; Hanson, W. B.; Seiff, A.; McElroy, M. B.; Spencer, N. W.; Duckett, R. J.; Knight, T. C. D.; and Cook, W. S.: Composition and Structure of the Martian Atmosphere: Preliminary Results From Viking 1. Science, vol. 193, no. 4255, Aug. 27, 1976, pp. 786-788.

2. Seiff, Alvin; and Kirk, Donn B.: Structure of the Atmosphere of Mars in Summer at Mid-Latitudes. J. Geophys. Res., vol. 82, no. 28, Sept. 30, 1977, pp. 4364-4378.

3. Seiff, Alvin; and Kirk, Donn B.: Structure of Mars' Atmosphere Up to 100 Kilometers From the Entry Measurements of Viking 2. Science, vol. 194, no. 4271, Dec. 17, 1976, pp. 1300-1303.

4. Zurek, Richard W.: Diurnal Tide in the Martian Atmosphere. J. Atmos. Sci., vol. 33, no. 2, Feb. 1976, pp. 321-337.

5. Lindzen, R. S.: Thermally Driven Diurnal Tide in the Atmosphere. Q. J. R. Meteorol. Soc., vol. 93, no. 395, Jan. 1967, pp. 18-42.

6. Soffen, G. A.; and Snyder, C. W.: The First Viking Mission to Mars. Science, vol. 193, no. 4255, Aug. 27, 1976, pp. 759-765.

7. Entry Data Analysis for Viking Landers 1 and 2. NASA CR-159388, 1976.

8. Hayes, Wallace D.; and Probstein, Ronald F.: Hypersonic Flow Theory. Academic Press, Inc., pp. 384-386.

9. Probstein, Ronald F.; and Kemp, Nelson H.: Viscous Aerodynamic Characteristics in Hypersonic Rarefied Gas Flow. J. Aero/Space Sci., vol. 27, no. 3, Mar. 1960, pp. 174-192.

10. Kennard, Earle H.: Kinetic Theory of Gases. McGraw-Hill Book Co., Inc., c.1938, p. 149.

11. Nicolet, W. E.: User's Manual for the Generalized Radiation Transfer Code (RAD/EQUIL). Rep. No. UM-69-9 (Contract NAS1-9399), Aerotherm Corp., Oct. 1, 1969. (Available as NASA CR-116353.)

12. Nier, A. O.; and McElroy, M. B.: Composition and Structure of Mars' Upper Atmosphere: Results From the Neutral Mass Spectrometer on Viking 1 and 2. J. Geophys. Res., vol. 82, no. 28, Sept. 30, 1977, pp. 4341-4349.

13. Miller, Charles G., III: Shock Shapes on Blunt Bodies in Hypersonic-Hypervelocity Helium, Air, and CO_2 Flows, and Calibration Results in Langley 6-Inch Expansion Tube. NASA TN D-7800, 1975.

14. Hurlbut, F. C.; and Sherman, F. S.: Application of the Nocilla Wall Reflection Model to Free-Molecule Kinetic Theory. Phys. Fluids, vol. 11, no. 3, Mar. 1968, pp. 486-496.

15. Nocilla, Silvio: The Surface Re-Emission Law in Free Molecule Flow. Rarefied Gas Dynamics, Volume I, J. A. Laurmann, ed., Academic Press, 1963, pp. 327-346.

16. Kinslow, Max; and Potter, J. Leith: Drag of Spheres in Rarefied Hypervelocity Flow. AIAA J., vol. 1, no. 11, Nov. 1963, pp. 2467-2473.

17. Svehla, Roger A.: Estimated Viscosities and Thermal Conductivities of Gas at High Temperatures. NASA TR R-132, 1962.

18. Hunt, James L.; Jones, Robert A.; and Midden, Raymond E.: Simulation of Real-Gas Effects for Mars Entry. J. Spacecr. & Rockets, vol. 11, no. 1, Jan. 1974, pp. 62-64.

19. Intrieri, Peter F.; DeRose, Charles E.; and Kirk, Donn B.: Flight Characteristics of Probes in the Atmospheres of Mars, Venus, and the Outer Planets. IAF-76-076, Oct. 1976.

20. Masson, D. J.; Morris, D. N.; and Bloxsom, Daniel E.: Measurements of Sphere Drag From Hypersonic Continuum to Free-Molecule Flow. U.S. Air Force Proj. RAND Res. Mem. 2678, Nov. 3, 1960.

21. Seiff, Alvin: The Viking Atmosphere Structure Experiment - Techniques, Instruments, and Expected Accuracies. Space Sci. Instrum., vol. 2, 1976, pp. 381-423.

22. Potter, J. Leith; Kinslow, Max; and Boylan, David E.: An Influence of the Orifice on Measured Pressures in Rarefied Flow. AEDC-TDR-64-175, U.S. Air Force, Sept. 1964.

23. Guy, R. W.; and Winebarger, R. M.: Effect of Orifice Size and Heat Transfer Rate on Measured Static Pressure in a Low-Density Arc-Heated Wind Tunnel. NASA TN D-3829, 1967.

24. Nier, Alfred O.; Hanson, William B.; McElroy, Michael B.; Seiff, Alvin; and Spencer, Nelson W.: Entry Science Experiments for Viking 1975. Icarus, vol. 16, no. 1, 1972, pp. 74-91.

25. Hanson, W. B.; Sanatani, S.; and Zuccaro, D. R.: The Martian Ionosphere as Observed by the Viking Retarding Potential Analyzers. J. Geophys. Res., vol. 82, no. 28, Sept. 30, 1977, pp. 4351-4363.

26. Schaaf, S. A.; and Chambre, P. L.: Flow of Rarefied Gases. Fundamentals of Gas Dynamics, Howard W. Emmons, ed., Princeton Univ. Press, 1958, pp. 687-738.

27. Moe, Kenneth: Recent Experimental Evidence Bearing on Satellite Drag Coefficients. AIAA J., vol. 6, no. 7, July 1968, pp. 1375-1377.

28. Boring, J. W.; and Humphris, R. R.: Drag Coefficients for Free Molecule Flow in the Velocity Range 7-37 km/sec. AIAA J., vol. 8, no. 9, Sept. 1970, pp. 1658-1662.

29. Schamberg, Richard E.: A New Analytic Representation of Surface Interaction for Hyperthermal Free Molecule Flow With Application to Neutral-Particle Drag Estimates of Satellites. U.S. Air Force Proj. RAND Res. Mem. RM-2313 (DTIC Doc. No. AD 215 301), RAND Corp., Jan. 8, 1959.

30. Cook, G. E.: Satellite Drag Coefficients. Planet & Space Sci., vol. 13, no. 10, Oct. 1965, pp. 929-946.

31. Cook, G. E.: Drag Coefficients of Spherical Satellites. Ann. Géophys. t. 22, nr. 1, Jan. 1966, pp. 53-64.

32. Öpik, Ernst J.: Physics of Meteor Flight in the Atmosphere, Interscience Publ., Inc., 1958.

33. Oman, Richard A.; Bogan, Alexander; and Li, Chou H.: Theoretical Prediction of Momentum and Energy Accommodation for Hypervelocity Gas Particles on an Ideal Crystal Surface. Rarefied Gas Dynamics, Volume II, J. H. De Leeuw, ed., Academic Press, 1966, pp. 396-416.

34. Oman, Richard A.; Bogan, Alexander; Weiser, Calvin H.; and Li, Chou H.: Interactions of Gas Molecules With an Ideal Crystal Surface. AIAA J., vol. 2, no. 10, Oct. 1964, pp. 1722-1730.

35. Hurlbut, F. C.: Current Developments in the Study of Gas-Surface Interactions. Rarefied Gas Dynamics, Volume I, C. L. Brundin, ed., Academic Press, 1967, pp. 1-34.

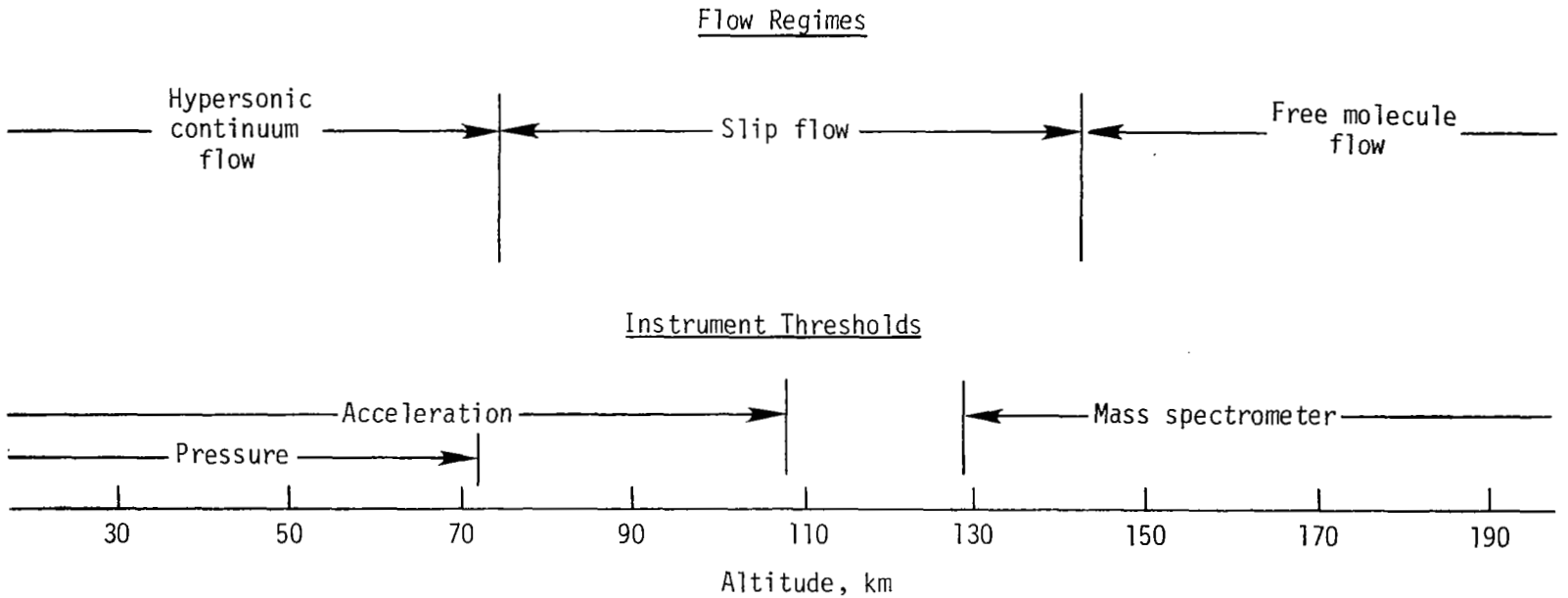

Figure 1.- Sketch of relationship between approximate thresholds of Viking Lander Capsule 1 measurements and flow regimes.

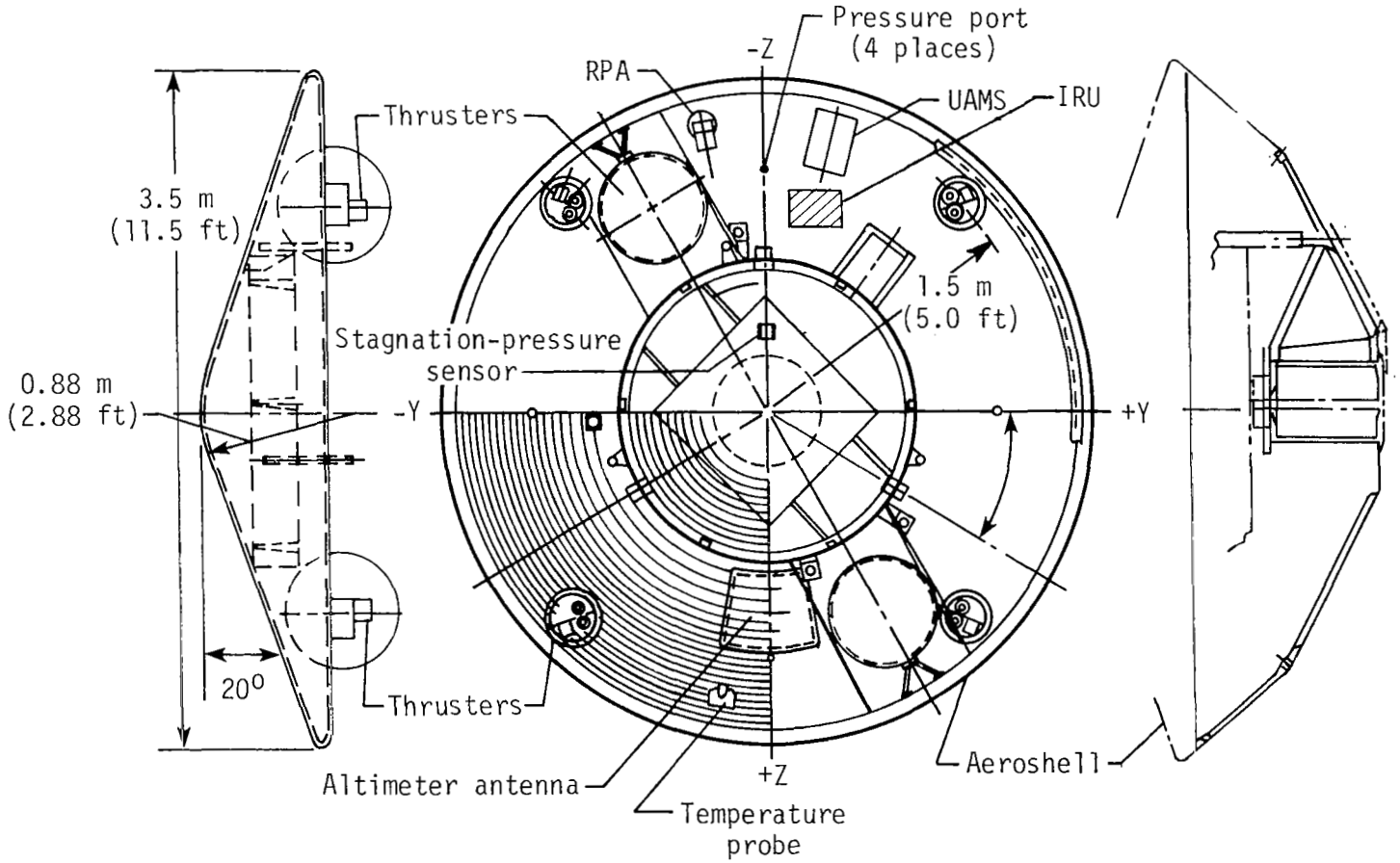

Figure 2.- Viking lander capsule aeroshell/base-cover configuration and instrumentation.

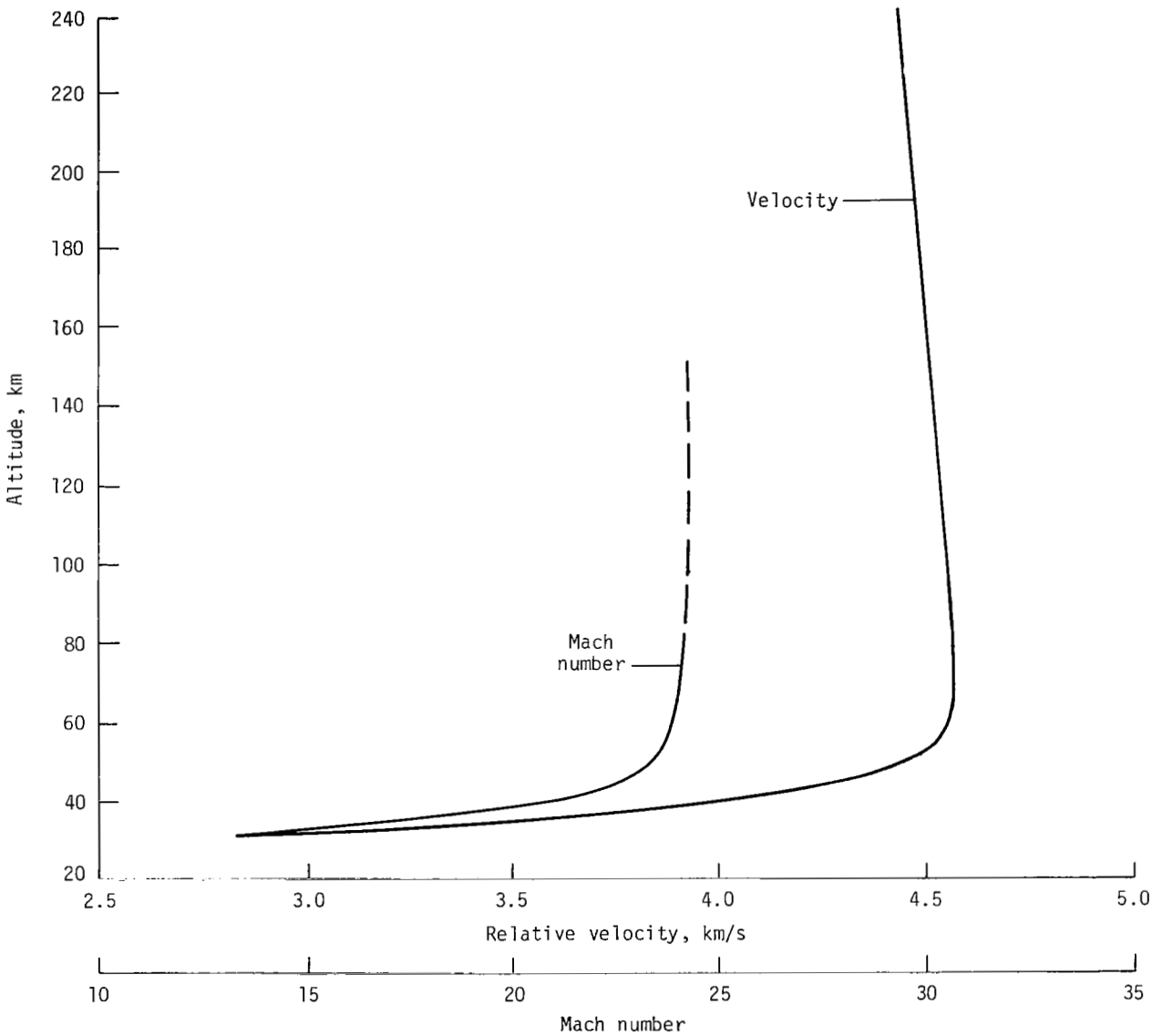

Figure 3.- Viking Lander Capsule 1 reconstructed velocity and approximate Mach number altitude profile.

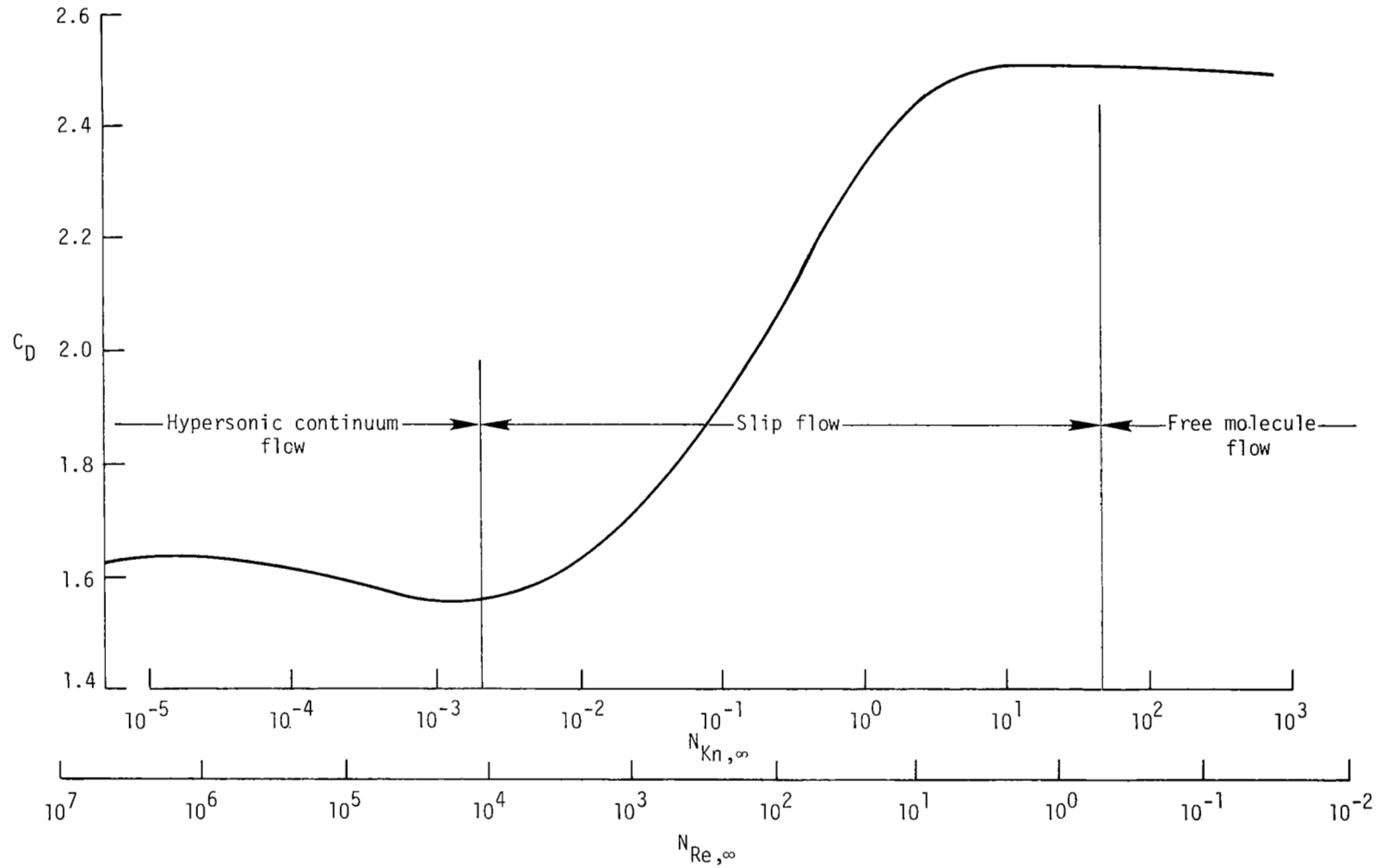

Figure 4.- Low-density flow regimes and drag coefficient for Viking lander capsule.

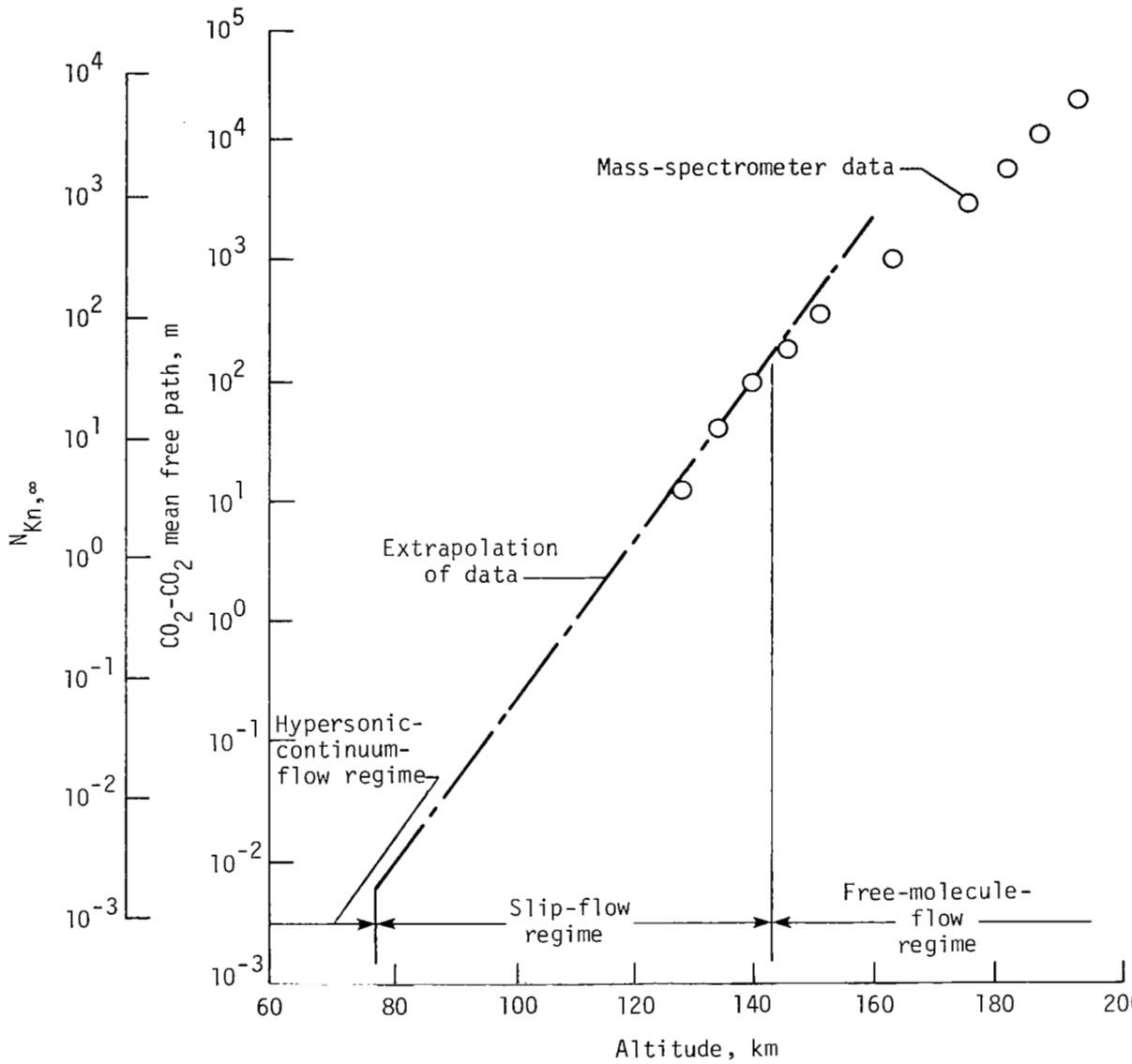

Figure 5.- Mean-free-path profile based on CO_2 collisions.

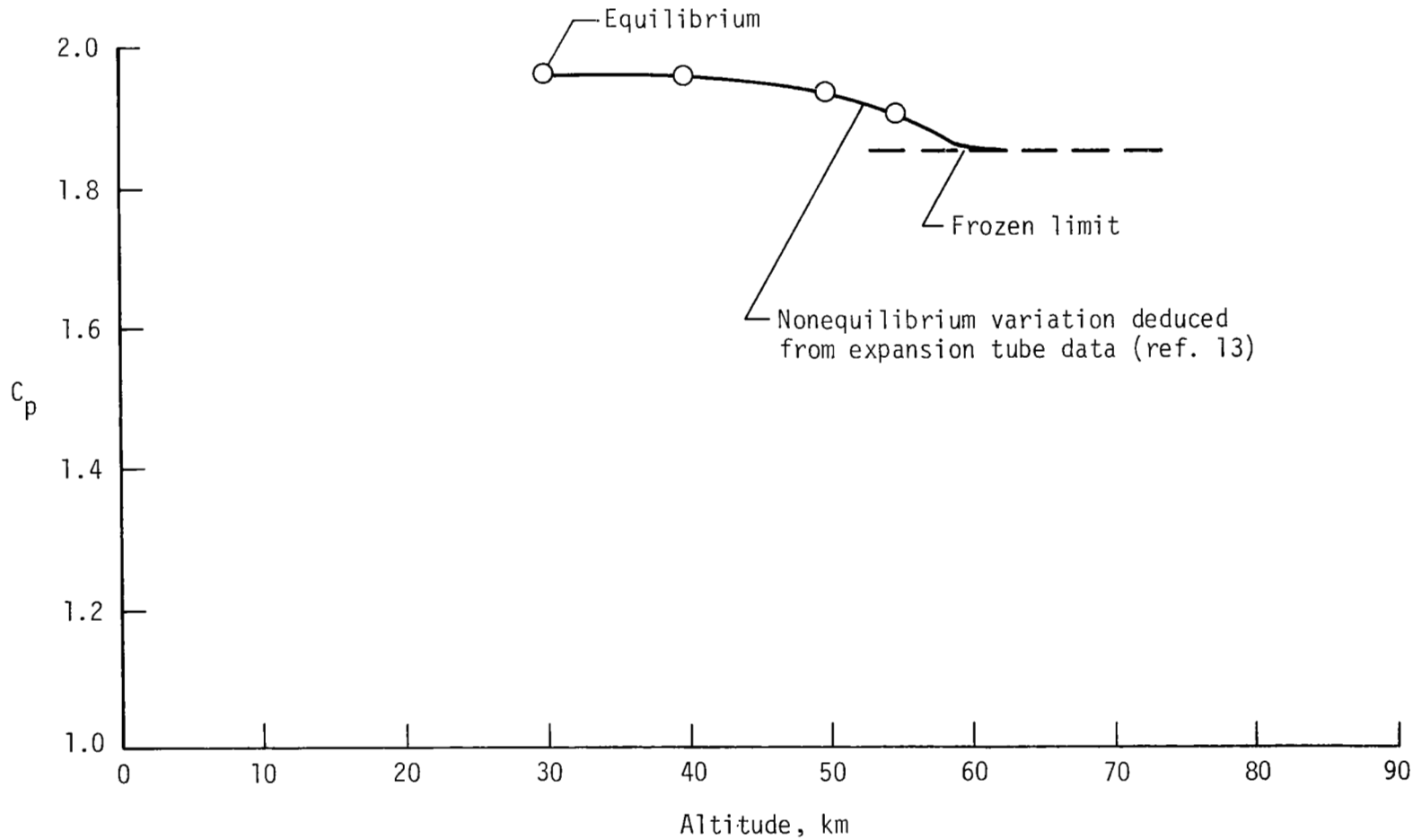

Figure 6.- Effect of flow nonequilibrium on variation of hypersonic stagnation pressure coefficient with altitude.

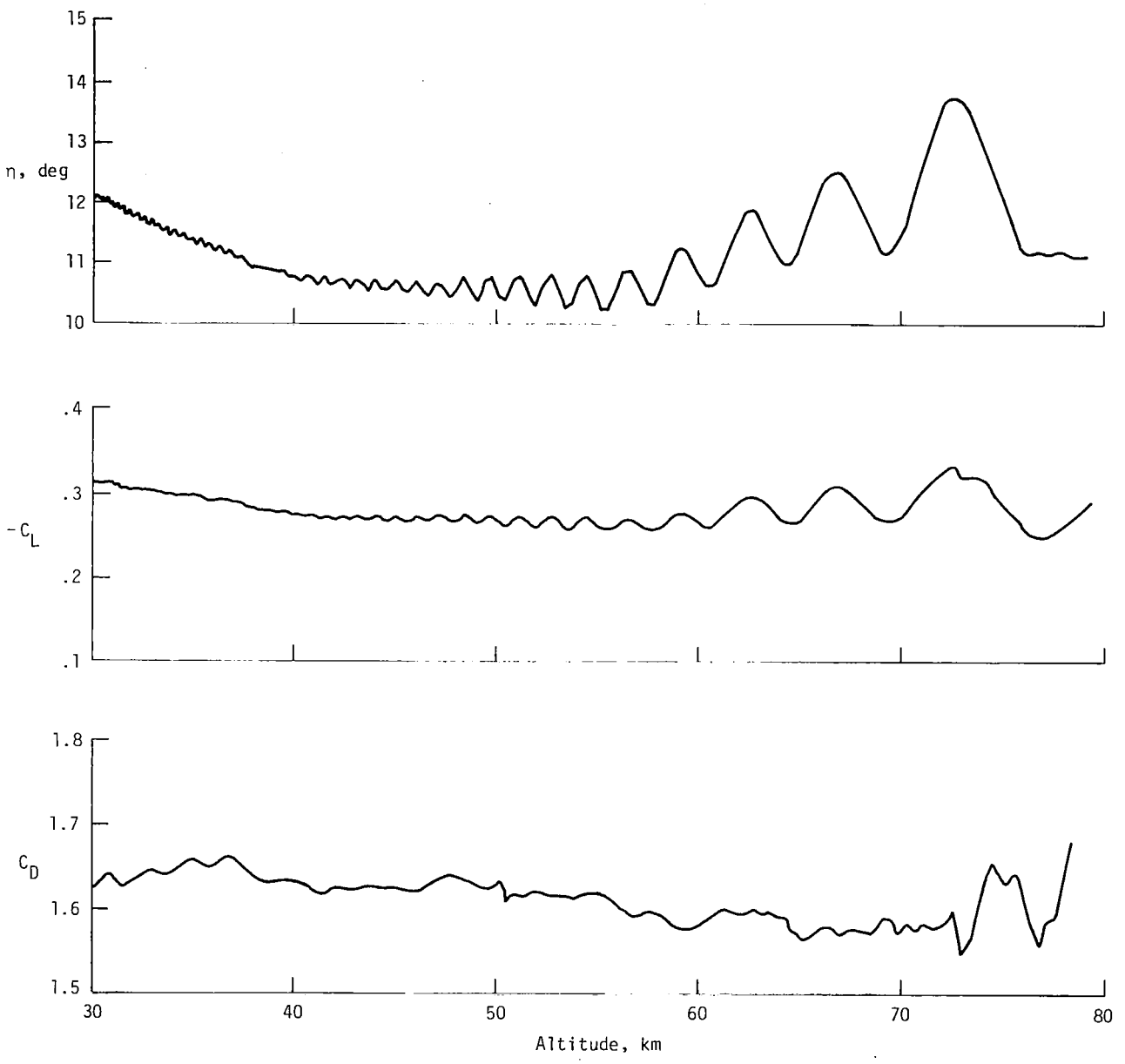

Figure 7.- Wind-vector force coefficients and angle of attack of the Viking Lander Capsule 1 determined from pressure, acceleration, and gyro data.

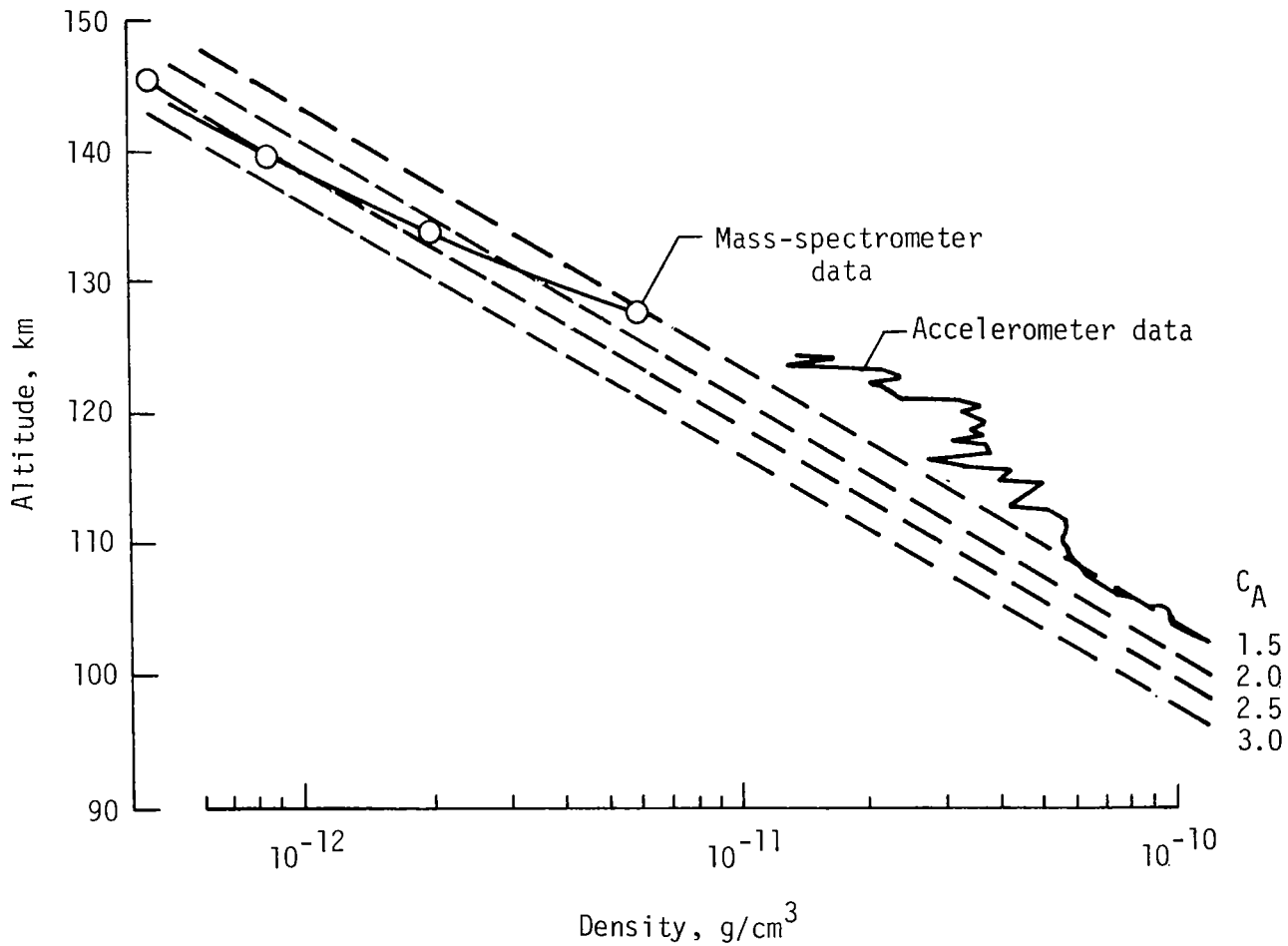

Figure 8.- Calculated density-altitude profiles for differing C_A along with mass-spectrometer and accelerometer data.

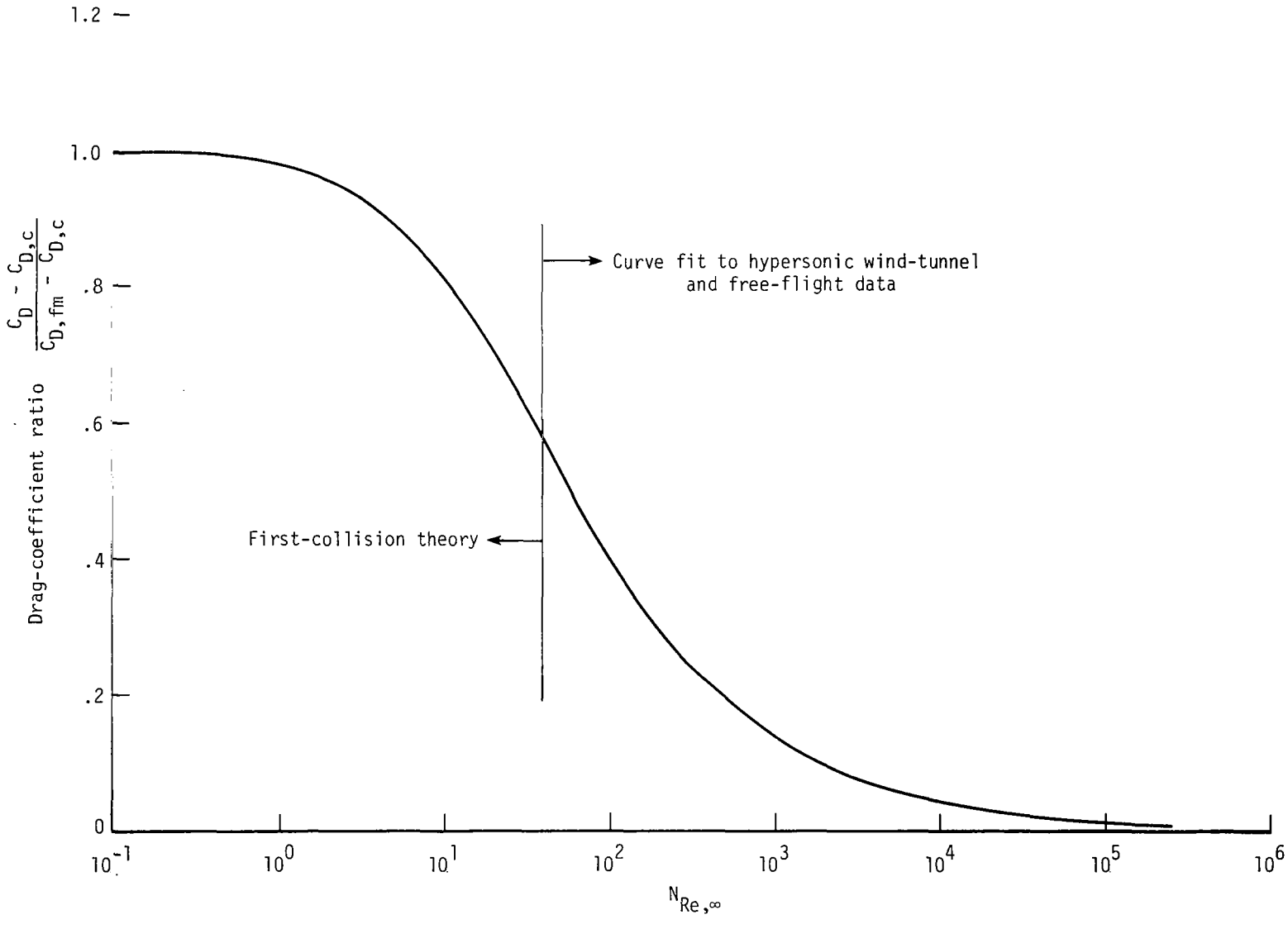

Figure 9.- Slip-flow drag coefficient variation for a sphere (ref. 16).

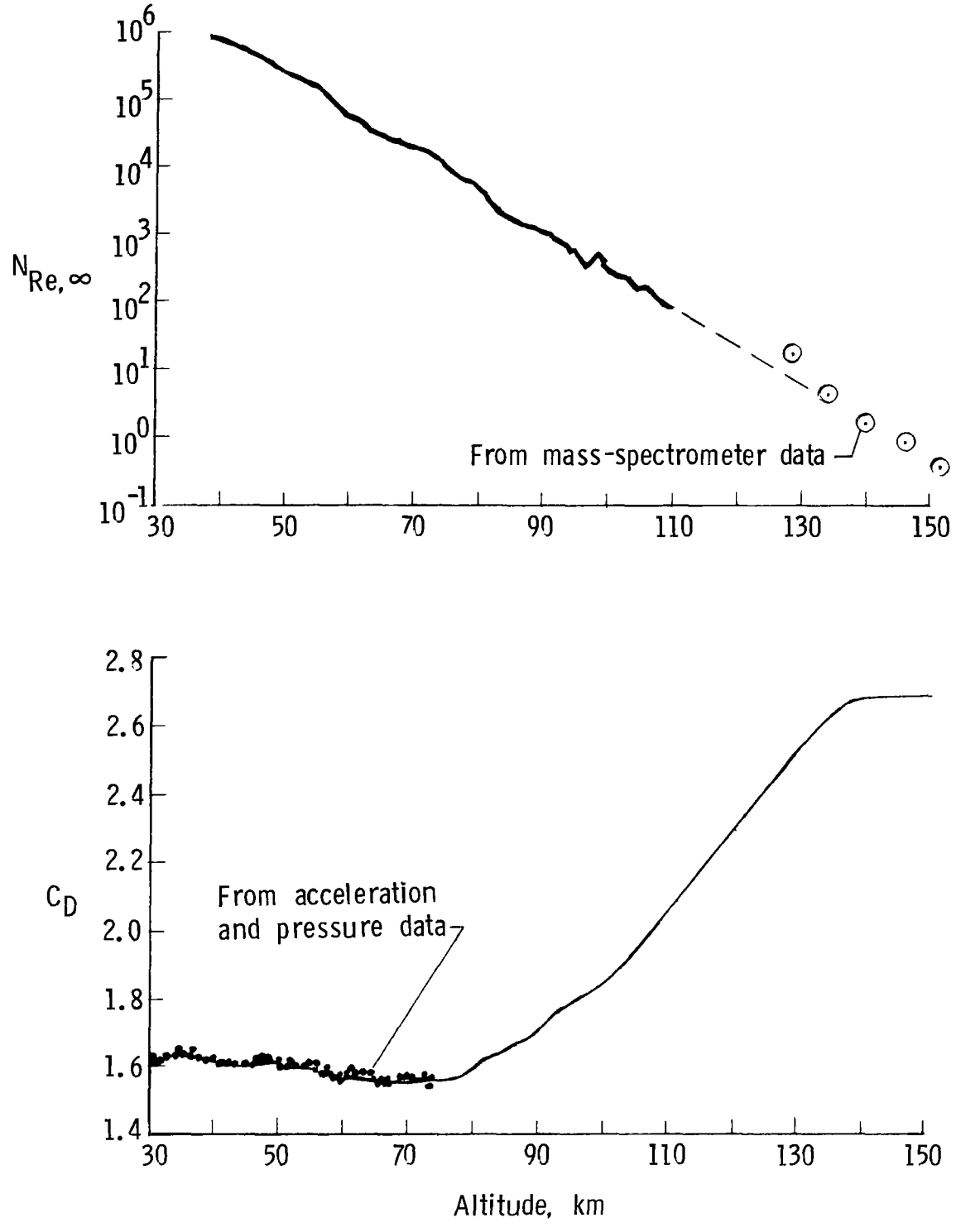

Figure 10.- The overall Viking Lander Capsule 1 drag-coefficient and free-stream Reynolds number altitude variation obtained from flight data.

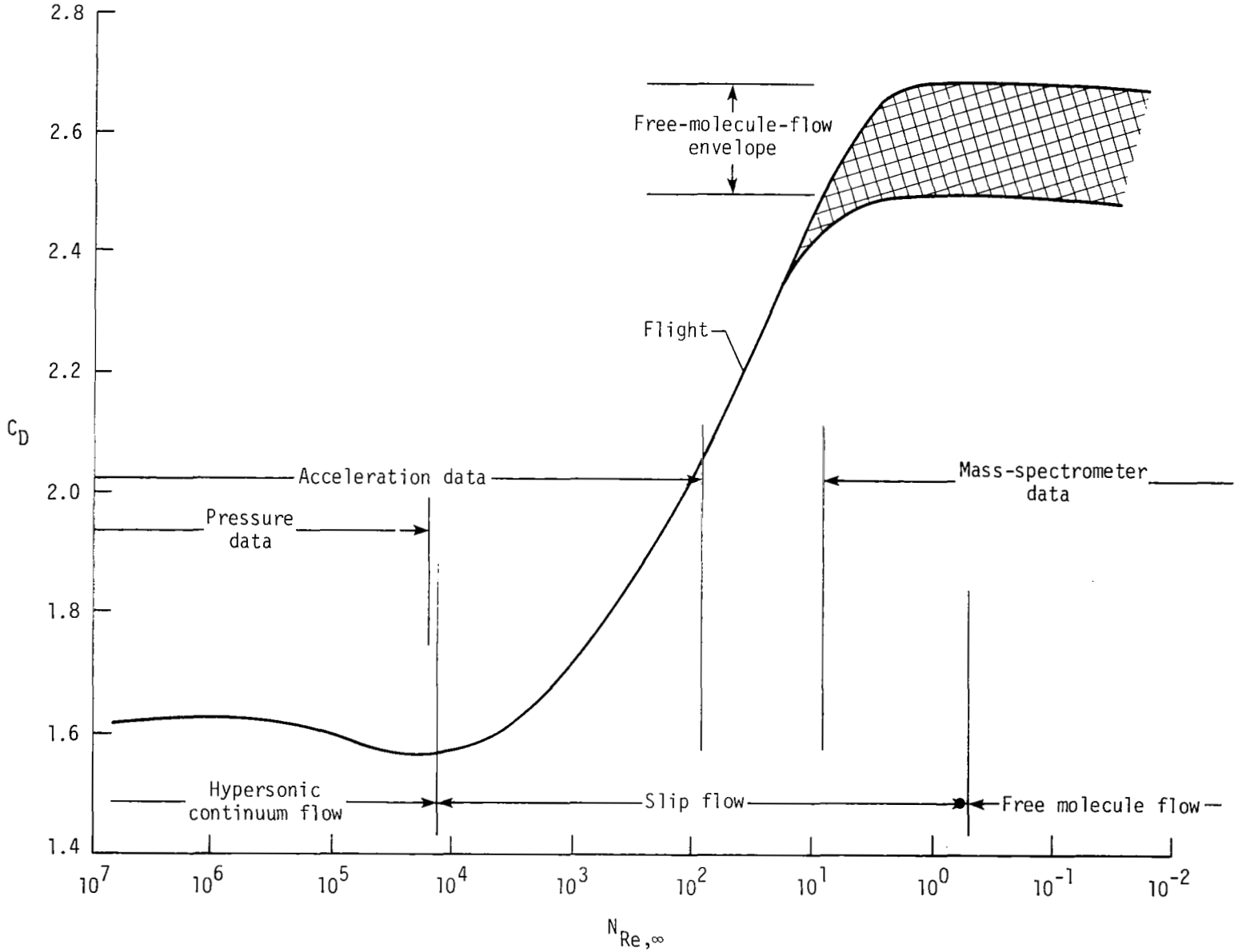

Figure 11.- Comparison of the complete drag-coefficient variation with flow regimes and approximate measurement thresholds of the data.

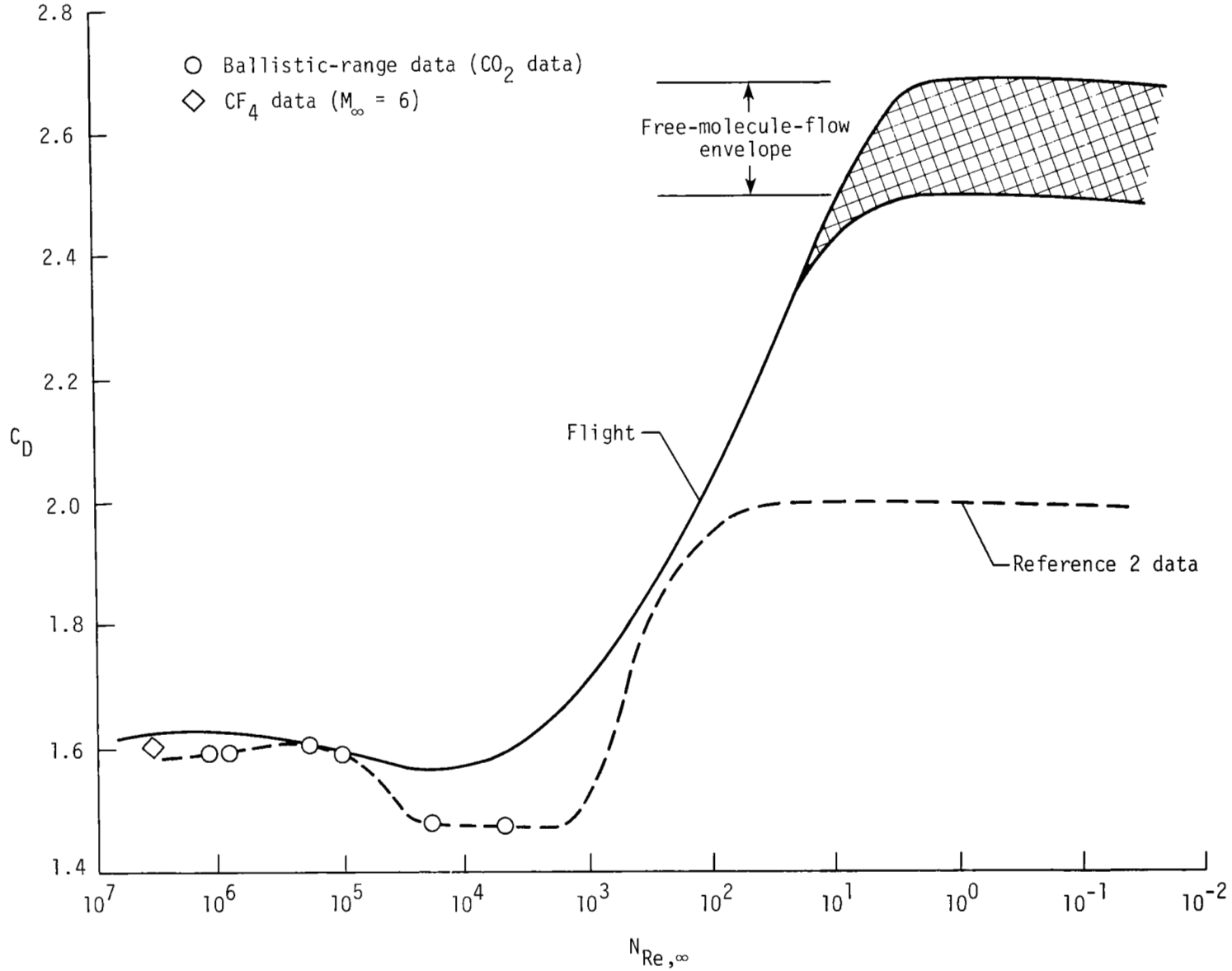

Figure 12.- Comparison of flight-derived drag-coefficient variation with wind-tunnel data.

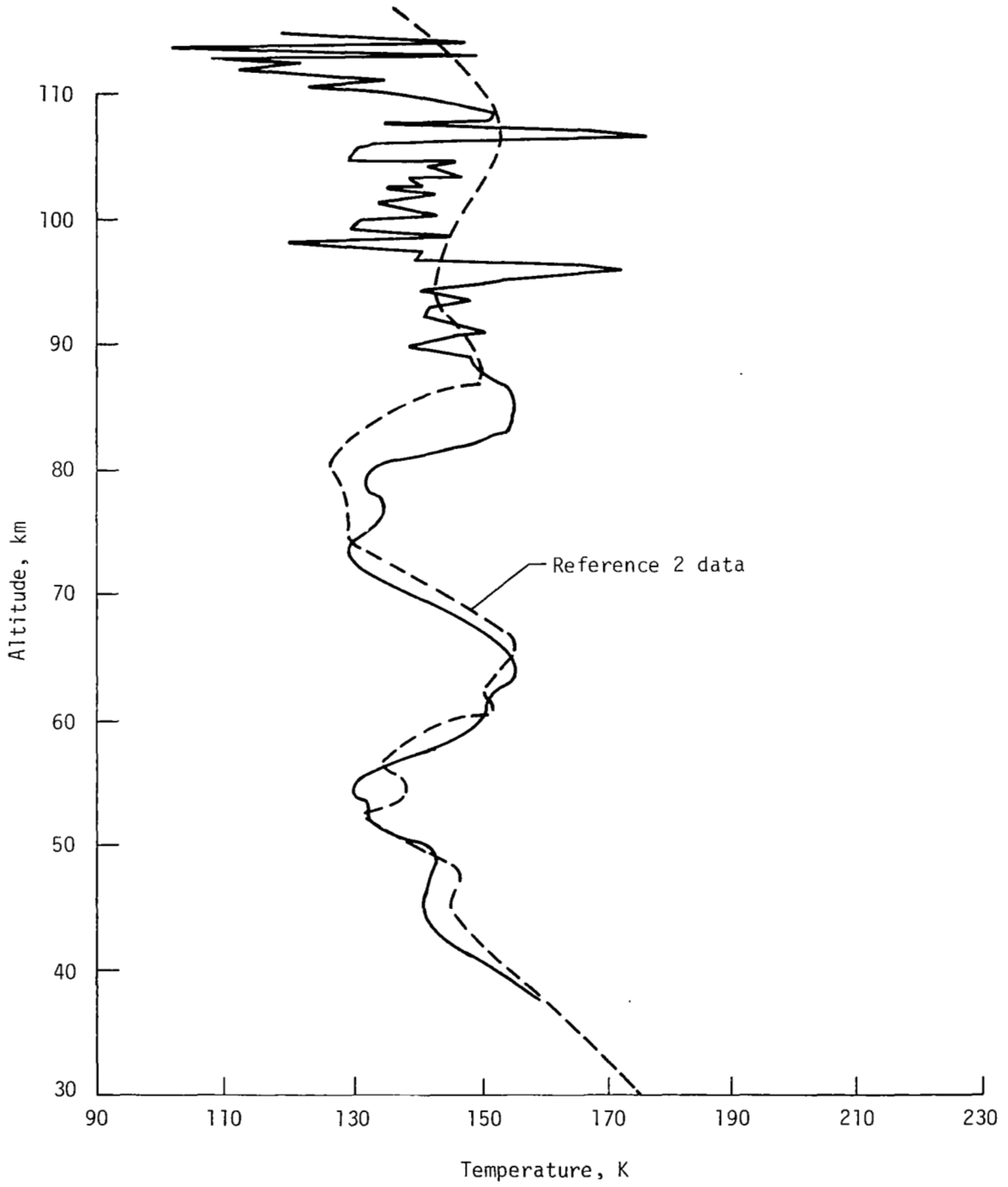

Figure 13.- Comparison of Mars atmospheric temperature profiles from Viking Lander Capsule 1 flight-derived and ground-test aerodynamics.

1. Report No.	2. Government Accession No.	3. Recipient's Catalog No.
NASA TP-1793		

4. Title and Subtitle	5. Report Date
DETERMINATION OF THE HYPERSONIC-CONTINUUM/RAREFIED-FLOW DRAG COEFFICIENTS OF THE VIKING LANDER CAPSULE 1 AEROSHELL FORM FLIGHT DATA	December 1980
	6. Performing Organization Code 506-51-33-01

7. Author(s)	8. Performing Organization Report No.
Robert C. Blanchard and Gerald D. Walberg	L-14042
	10. Work Unit No.

9. Performing Organization Name and Address	11. Contract or Grant No.
NASA Langley Research Center Hampton, VA 23665	
	13. Type of Report and Period Covered

12. Sponsoring Agency Name and Address	13. Type of Report and Period Covered
National Aeronautics and Space Administration Washington, DC 20546	Technical Paper
	14. Sponsoring Agency Code

15. Supplementary Notes

16. Abstract

Results of an investigation to determine the full-scale drag coefficient in the high-speed, low-density regime of the Viking Lander Capsule 1 entry vehicle are presented. The principal flight data used in the study were from onboard pressure, mass-spectrometer, and accelerometer instrumentation. The hypersonic-continuum-flow drag coefficient was unambiguously obtained from pressure and accelerometer data; the free-milecule-flow drag coefficient was indirectly estimated from accelerometer and mass-spectrometer data; the slip-flow drag-coefficient variation was obtained from an appropriate scaling of existing experimental sphere data. Analyses of the flight data are included as appendixes. Comparison of the flight-derived drag coefficients with ground-test data generally showed good agreement in the hypersonic-continuum-flow regime except for Reynolds numbers from 10^5 to 10^3, for which an unaccountable difference between flight-and ground-test data of about 8 percent existed. The flight-derived drag coefficients in the free-molecule-flow regime were considerably larger than those previously calculated with classical theory. The general character of the previously determined temperature profile was not changed appreciably by the results of this investigation; however, a slightly more symmetrical temperature variation at the highest altitudes was obtained.

17. Key Words (Suggested by Author(s))	18. Distribution Statement
Aerodynamics Entry-data analysis Rarefied flow Mars entry data Viking Lander 1 aeroshell	Unclassified - Unlimited Subject Category 01

19. Security Classif. (of this report)	20. Security Classif. (of this page)	21. No. of Pages	22. Price
Unclassified	Unclassified	57	A04

For sale by the National Technical Information Service, Springfield, Virginia 22161

NASA-Langley, 1980